7 Electron and photon identification and measurement

7.1 Introduction

The emphasis of this chapter is a discussion of how the combination of the Inner Detector (ID) and the EM Calorimeter (and to a lesser extent, the Hadronic Calorimeter) can be used to identify and measure electrons and photons. Performance obtained using either the ID or the EM Calorimeter alone is described in the corresponding chapters, namely Chapter 3 or Chapter 4. For example, the electron-pion separation using transition radiation (TR) is described in Section 3.4. In this chapter, strategies for identifying electrons and photons originating from different physical processes in the presence of appropriate backgrounds are discussed. Methods for improving measurements are also presented. In what follows, it is clear that analyses will be improved as a better understanding of the detector is gained and new software is developed. Throughout this chapter, 'low luminosity' will be used to imply no pile-up.

7.2 Electron measurements

7.2.1 Measurements in the Inner Detector

As can be seen from Figure 3-5, there is a significant amount of material in the ID. The total material in the active volume of the ID averaged over $|\eta| < 2.5$ is ~50% X_0, hence there is a sizeable probability for an electron to loose a significant fraction of its energy before leaving the ID. Although much of the bremsstrahlung radiation will be collected by the EM Calorimeter, the track in the ID may be seriously affected causing its p_T to be poorly reconstructed and in some cases, making it difficult to reconstruct the track at all. The probabilities for electrons to radiate a given fraction of their energies are shown in Figures 7-1 and 7-2. For example, 20% of electrons will have lost half of their energy by the time they leave the ID barrel. The distributions are shown for p_T = 20 GeV electrons, however, the p_T dependence is small.

7.2.1.1 Bremsstrahlung recovery procedures

The track parameters reconstructed from a set of hits in the ID are not uniquely defined, but depend on the fitting procedure. Adjustments are possible using the ID information alone and further improvements to the track parameters can be made by using the EM cluster centroid as an external point. By allowing for bremsstrahlung on an electron track, it is possible to recover some of the efficiency losses which occur with a simple fit tuned for muons. In the following, the recovery procedures adopted by three of the ID pattern recognition programs (see Section 3.1.2) are discussed.

PixlRec allows for a discreet change of curvature at a fitted radius resulting in a seven parameter fit. For tracks where the fraction of TR hits exceeds 15%, xKalman attempts to recover from the energy loss by bremsstrahlung by incorporating it as an additional noise term in the Kalman Filtering formalism, in a manner akin to the multiple-scattering treatment. The modified track

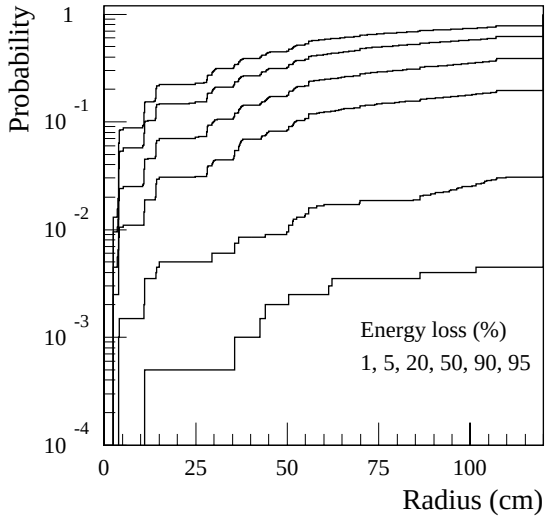

Figure 7-1 Probability that an electron with |η| = 0.3 (ID barrel) will radiate a given fraction of its energy within a certain radius. (Upper lines correspond to smaller losses.)

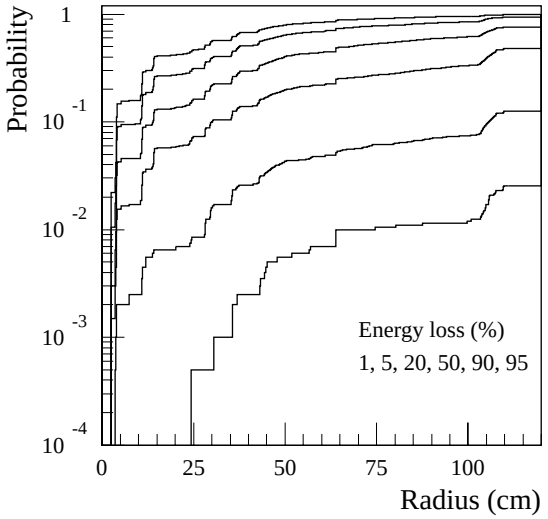

Figure 7-2 Probability that an electron with |η| = 1.3 (ID barrel/end-cap overlap) will radiate a given fraction of its energy within a certain radius. (Upper lines correspond to smaller losses.)

fit is retained if the track quality, measured by the number of precision hits, is improved (default operation). There exists in iPatRec, the possibility to fit the track in just the first few silicon layers, thereby reducing the sensitivity to the bremsstrahlung. By giving more weight to the earlier part of the track, all of these methods reduce the sensitivity to bremsstrahlung at the cost of reduced p_T resolution.

It can be shown that in the case of a single hard radiation, the energy-weighted barycentre of the impact points of the electron and the photon in the EM Calorimeter lies on the extrapolation of the initial electron trajectory. When the bremsstrahlung photon and the final electron both leave the ID with sufficient energy, these energy deposits merge into a single EM cluster. Hence, in principle, an unbiassed estimate of the original electron energy can be deduced from a helical fit using the track segment before the radiation and including the EM cluster barycentre. xKalman uses this principle to improve the p_T estimate by minimising a χ^2 containing all the fitted track information and the EM cluster position.

7.2.1.2 Momentum measurement in the Inner Detector

Electrons with p_T = 20 GeV were reconstructed with iPatRec, and fitted using all the track information (including the TRT) or just the information from the first four or five silicon planes. The ratio of the true p_T to the reconstructed p_T was formed and the core of the distribution was fitted with a Gaussian. The means and sigmas of the fits are shown as a function of pseudorapidity in Figures 7-3 and 7-4 respectively. It can be seen that as the track is truncated, the mean is closer to unity, indicating that there is less sensitivity to bremsstrahlung, but the resolution is degraded. The results of the fit to the complete track are very similar to those obtained with xKalman.

Figures 7-5, 7-6 and 7-7 illustrate different bremsstrahlung recovery procedures implemented in the xKalman program for p_T = 20 GeV electrons in the barrel. Gaussian fits were made to the cores ($\pm 1.5\sigma$) of the distributions of the ratio of true p_T to reconstructed p_T. Figure 7-5 shows the ratios obtained using the 'muon-fit', which is appropriate for muons, but makes no allowance for electron bremsstrahlung. The tail corresponding to lower reconstructed p_T is clear. Figure 7-

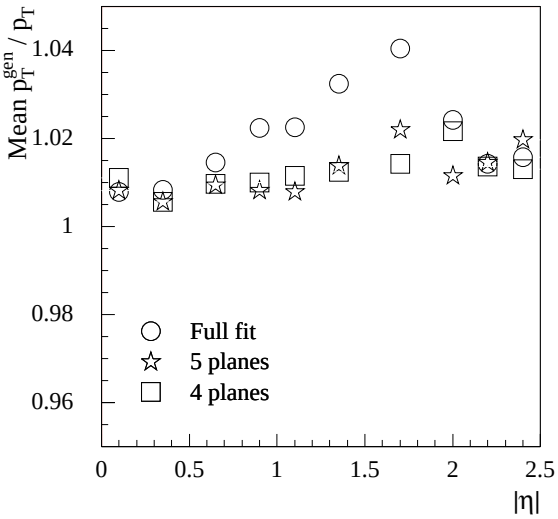

Figure 7-3 Ratio of true p_T to reconstructed p_T for p_T = 20 GeV electrons reconstructed by iPatRec. The means are obtained from Gaussian fits to the cores of the distributions as a function of pseudorapidity. Track fits are made to either the full track or a reduced number of silicon planes.

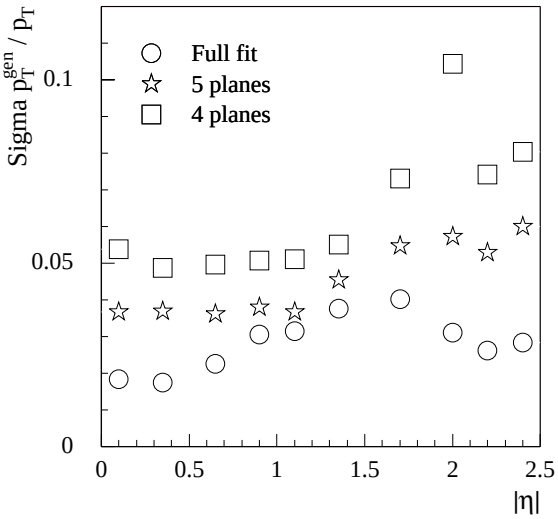

Figure 7-4 Resolution of reconstructed p_T for p_T = 20 GeV electrons reconstructed by iPatRec. The sigmas are obtained from Gaussian fits to the cores of the distributions as a function of pseudorapidity. Track fits are made to either the full track or a reduced number of silicon planes.

6 shows the ratios obtained using the 'electron fit', which does allow for radiation. The distribution is far more Gaussian, but with worse p_T resolution. Figure 7-7 shows the ratios obtained using the muon-fit combined with the EM cluster position. Although there is a tendency to overcompensate for the increased curvature, the tails have been reduced while retaining the resolution of the muon-fit.

The emphasis of the bremsstrahlung recovery algorithms in xKalman is to follow the track through the ID so as to associate as many hits as possible and to reduce the tails in the p_T distribution in order to increase the electron reconstruction efficiency. Figure 7-8 shows the efficiency for the different fitting procedures. The 'combined-fit' is the default fit for identified electrons, as described in the previous section. This corresponds to the combination of the muon and electron-fits, where the muon-fit is retained in most cases, but for the few percent of electrons where the number of precision hits on the track is increased, the electron-fit is kept. The efficiencies were evaluated for electrons passing the extended ID track quality cuts (see Section 3.1.3) and satisfying $0.7 < p_T^{gen} / p_T < 1.4$ (the results are not very sensitive to whether the normalisation is with respect to the true p_T or the E_T measured by the EM Calorimeter). The electron-fit increases the efficiency by ~6% with respect to the muon-fit, although it degrades the p_T resolution by a factor of ~2. The combined-fit increases the efficiency by ~2%, while retaining good resolution. The use of the EM cluster position significantly improves the tails and hence the efficiency at higher p_T. Around 200 GeV, the intrinsic ID resolution starts to dominate the bremsstrahlung tails and causes events to be lost by the cut on p_T^{gen} / p_T.

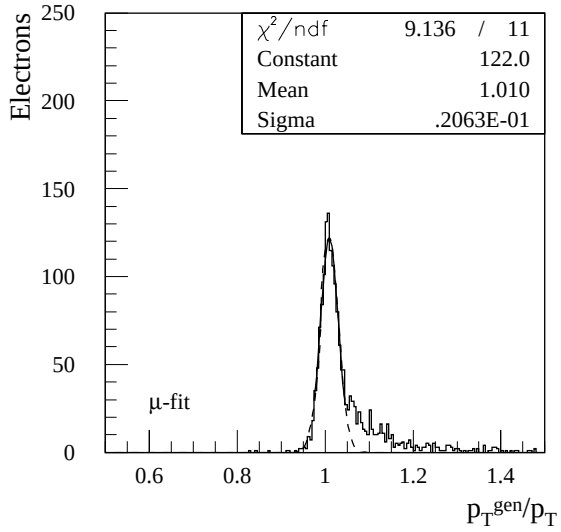

Figure 7-5 Ratio of true to reconstructed p_T from xKalman using the muon-fit for electrons with p_T = 20 GeV and η = 0.3.

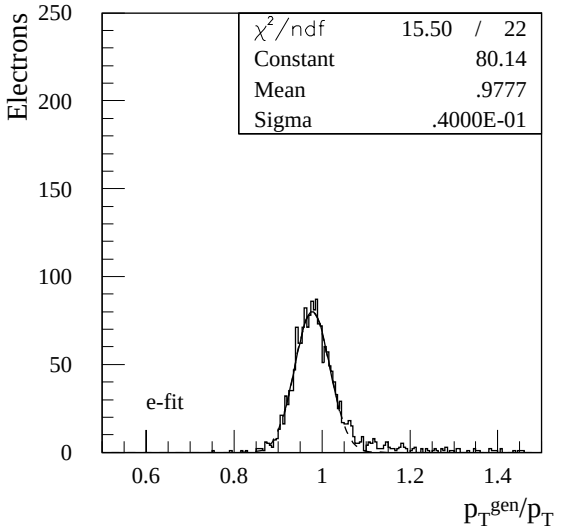

Figure 7-6 Ratio of true to reconstructed p_T from xKalman using the electron-fit for electrons with p_T = 20 GeV and η = 0.3.

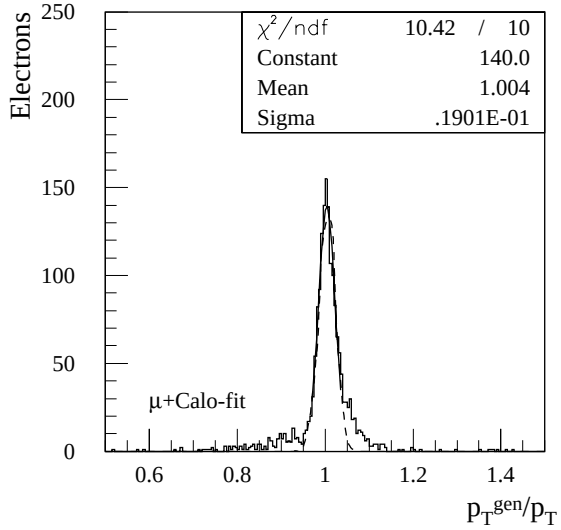

Figure 7-7 Ratio of true to reconstructed p_T from xKalman using the muon-fit along with the EM cluster position for electrons with p_T = 20 GeV and η = 0.3.

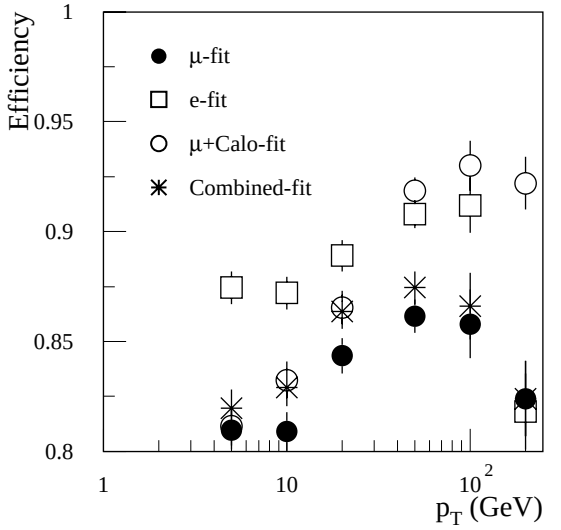

Figure 7-8 Efficiency for reconstructing electrons (η = 0.3) with xKalman using different fits. Electrons are required to satisfy the extended ID quality cuts and $0.7 < p_T^{gen}/p_T < 1.4$.

7.2.2 Matching the Inner Detector and EM Calorimeter

7.2.2.1 *E/p* for electron identification

The comparison between the momentum reconstructed in the ID and the energy measured in the EM Calorimeter is valuable in identifying electrons, as is demonstrated in subsequent sections. It also serves as an important source of calibration for the EM Calorimeter.

Figures 7-9 and 7-10 summarise the shapes of the *E/p* distributions as a function of pseudorapidity for p_T = 5 and 20 GeV electrons respectively. To give the narrowest distributions, full fits were made using all the track information. At p_T = 20 GeV, the width of the distributions is ~2.5%.

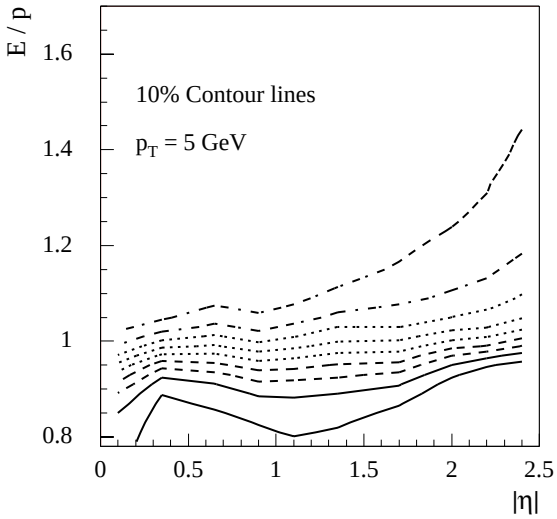

Figure 7-9 Contour plot showing value of *E/p* below which 10, 20, 30, 40, 50, 60, 70, 80 and 90% of electrons are reconstructed at given values of pseudorapidity. Curves are shown for p_T = 5 GeV electrons reconstructed with iPatRec using all the track information.

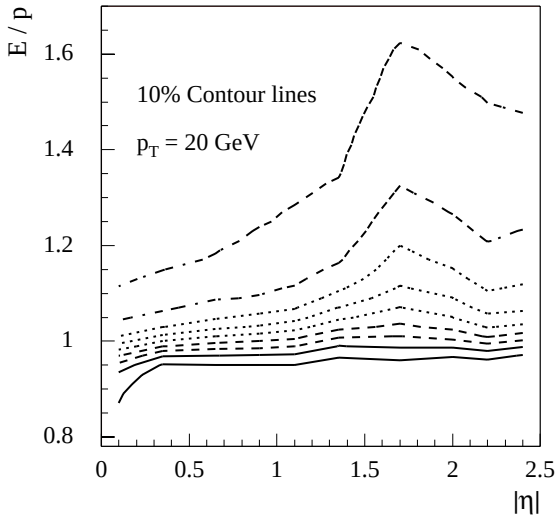

Figure 7-10 Contour plot showing value of *E/p* below which 10, 20, 30, 40, 50, 60, 70, 80 and 90% of electrons are reconstructed at given values of pseudorapidity. Curves are shown for p_T = 20 GeV electrons reconstructed with iPatRec using all the track information.

7.2.2.2 *E/p* for calibration of the EM Calorimeter

The main tool for calibrating the EM Calorimeter will be $Z \rightarrow ee$ events, as described in Chapter 4. The peak of the *E/p* distribution will provide a valuable cross-check of the calibration. As a precursor to this, it is essential that the momentum scale of the ID is correctly calibrated for muons along the lines discussed in Chapter 12. Subsequently, the calibration for electrons must be made, allowing for *dE/dx* losses and bremsstrahlung. These corrections will come from Monte Carlo studies like those illustrated in Figure 7-3, and hence will rely on a good model of the detector in the simulation and an accurate description of physical processes by GEANT.

The cores of the *E/p* distributions for different electron energies were fitted with Gaussians. The means and sigmas of the fits are shown as a function of pseudorapidity in Figures 7-11 and 7-12 respectively. The electrons have been reconstructed by iPatRec using the first four silicon planes to reduce the sensitivity to the bremsstrahlung. The mean values of *E/p* have a variation with pseudorapidity which comes primarily from the ID p_T (Figure 7-3). However, there are also some effects arising from imperfections in the Monte Carlo calibration of the Calorimeter, for example at E_T = 20 GeV, the energy calibration is about (1 ± 1)% too low.

The resolution which can be achieved on *E/p* (Figure 7-12) leads directly to estimates of how many events will be required to check the calibration of the EM Calorimeter. Taking the resolution to be 5%, 400 regions of the EM Calorimeter can be calibrated with a statistical precision of 0.1% with 10^6 electrons. This should not be a problem, since at low luminosity, it is anticipated that 30×10^6 reconstructed $W \rightarrow e\nu$ events will be collected in one year. The 5% resolution comes

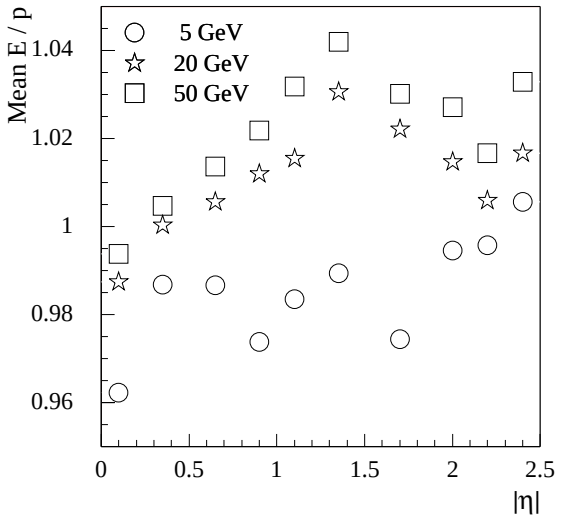

Figure 7-11 Ratio of *E/p* for electrons reconstructed by iPatRec. The means are obtained by fitting to the cores of the distributions as a function of pseudorapidity. Fits are made to the first four silicon planes.

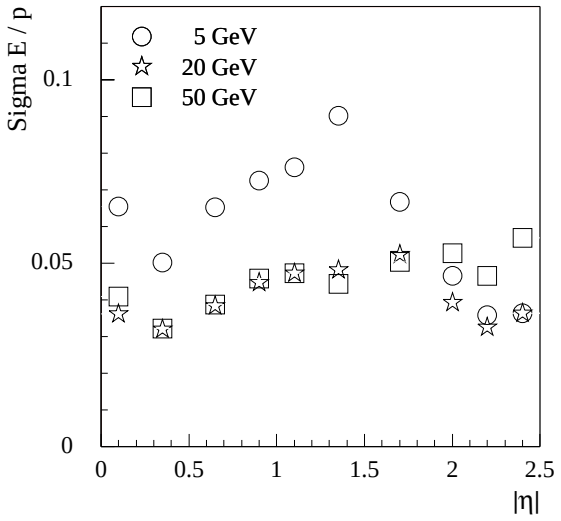

Figure 7-12 Resolution on *E/p* for electrons reconstructed by iPatRec. The sigmas are obtained by fitting to the cores of the distributions as a function of pseudorapidity. Fits are made to the first four silicon planes.

from the track fit to the first four or five silicon planes. If there is sufficient confidence in correcting for the effects of bremsstrahlung so that the full track information can be used, then the same statistical precision will be achieved with a quarter of the number of events.

7.2.2.3 Sensitivity to the material of the Inner Detector

The position of the *E/p* peak depends on the amount of material, especially that located at smaller radii. To test the sensitivity to this in the simulation, the material in the SCT support structures was increased. These structures (cylinders in the barrel and disks in the end-caps) are simulated as simple, uniform surfaces, on which the detectors are mounted. In the barrel, the material increased from 10% to 14.5% X_0. The corresponding change in the *E/p* distribution can be seen in Figure 7-13. There is a small shift in the peak of the distribution and the tail of the distribution has increased, with extra events around *E/p* = 1.3. With the 45% increase in material in the SCT, the peak has shifted by 0.0025, so if it is required to understand this shift at the level of 0.1%, the material of the SCT in the barrel must be understood to better than ~20% of its value - this will be easy. However, should it be desired to understand the shift at the 0.01% level, then the material must be known to ~2% – this will be far more challenging.

To cross-check the EM Calorimeter calibration at the 0.02% level using *E/p* will be possible only if the systematic effects mentioned earlier can be understood. If this can be done, then it will be necessary to determine the SCT material to ~2%. This requirement is likely to be even tighter for the Pixel System, which is located at small radius, and in the end-caps, where there is more material. The requirements for the Pixels will be examined in future studies.

The material in the ID can be estimated from direct calculation, the conversion rates (see Chapter 12) or from the *E/p* distribution itself. Different parts of the *E/p* distribution will be sensitive to bremsstrahlung from different radii. By making a fit to the distribution, which is sensitive to the different components, it should be possible to estimate the ID material by reference to simulation. Using this method, CDF understood the material in their tracker to 10% [7-1]. Clear-

ly, this will rely on having an accurate description of the physical processes associated with tracking electrons by GEANT as well as a good description of the detector. The distributions shown in Figure 7-13 were fitted over a slightly larger range ($\pm 1.5\sigma$) to increase the sensitivity to the effect of extra SCT material. One such fit is shown in Figure 7-14. The difference in the widths of the fitted Gaussians was 0.0052, with an uncertainty on measuring the width of 0.0007. To obtain a precision which is 25 times better would require a determination of the width to 0.0002. The uncertainty on the width was obtained with a sample of 8,800 reconstructed single electrons; to reduce this uncertainty to 0.0002 would require 1.0×10^5 reconstructed electrons. Similar calculations for the end-cap region ($|\eta| = 1.8$), indicate that approximately 2.2×10^5 electrons would be required. With 30×10^6 reconstructed $W \rightarrow e\nu$ events expected for each year of low luminosity running, this should allow a satisfactory determination of the ID material as a function of pseudorapidity. By using an inclusive electron sample (as obtained from the analysis of Section 7.4), larger numbers of electrons could be used. Although it will be more difficult to resolve deviations from the material expected at different radii, sensitivity to the different components should be possible by fitting the *E/p* distribution by functions with more parameters.

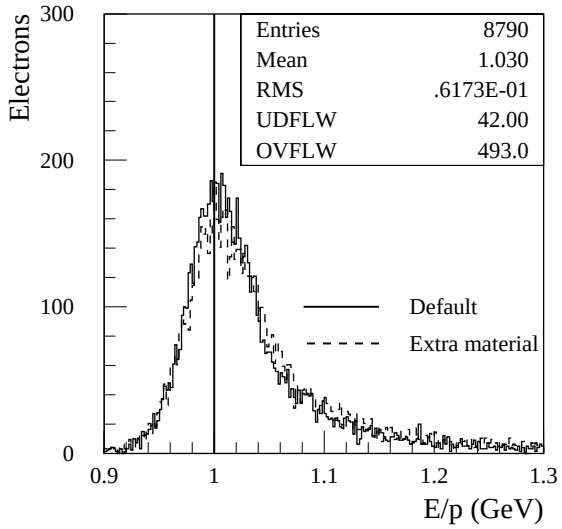

Figure 7-13 *E/p* distribution for single electrons with p_T = 20 GeV and η = 0.3, reconstructed by xKalman. The figure shows the distribution for the default layout as well as for a layout with 45% more material in the SCT.

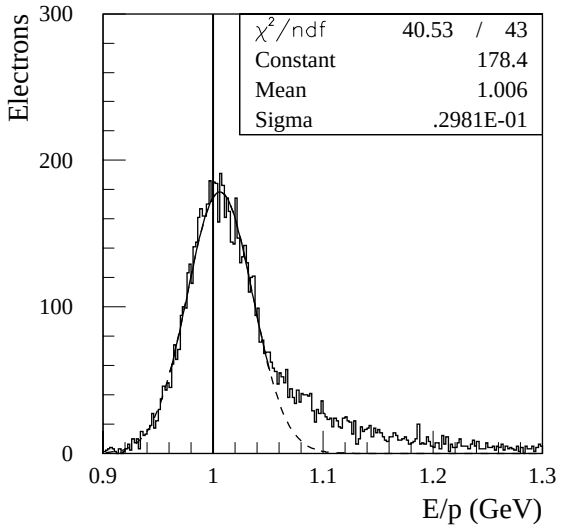

Figure 7-14 *E/p* distribution for single electrons with p_T = 20 GeV and η = 0.3, reconstructed by xKalman, for the default layout. Also shown is a Gaussian fit to $\pm 1.5\sigma$ around the peak.

7.2.2.4 Position matching

Tracks and clusters are associated by looking at the matching between the track direction and the corresponding calorimeter quantities. These are evaluated as follows:

- The pseudorapidity is computed from the position measured in the first compartment of the EM Calorimeter, an estimate of the shower depth in this compartment and the *z*-position along the beam line, which is measured by the ID with a negligible error.
- The azimuthal angle is computed from the position measured in the second compartment of the EM Calorimeter and an estimate of the shower depth in this compartment. The measured transverse energy is used to correct for the curvature of the electron trajectory in the magnetic field to give an estimate of the azimuthal direction at the beam line.

Figures 7-15 and 7-16 show the matching in pseudorapidity and azimuth for p_T = 20 GeV electrons, without electronic noise or pile-up. The dashed lines indicate the cuts which are used for electron / jet (see Section 7.4.2.3) and photon / electron (see Section 7.7.1) separation. At high luminosity, the probability to find a track from the pile-up with $p_T > 5$ GeV pointing to the $\Delta\eta = \pm 0.01$, $\Delta\phi = \pm 0.02$ window is about 10^{-4}.

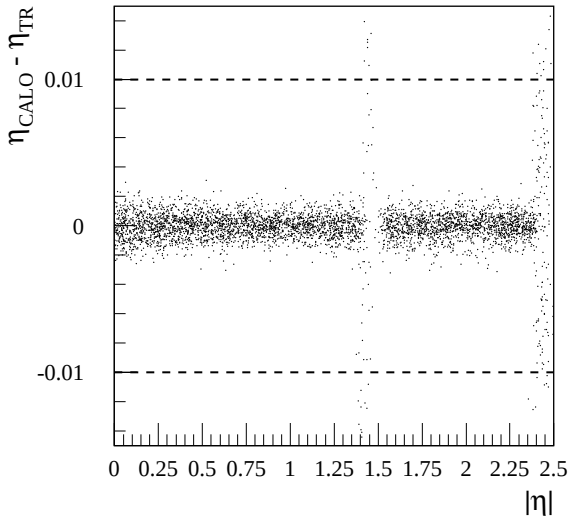

Figure 7-15 Matching in pseudorapidity between the EM Calorimeter and ID for p_T = 20 GeV electrons.

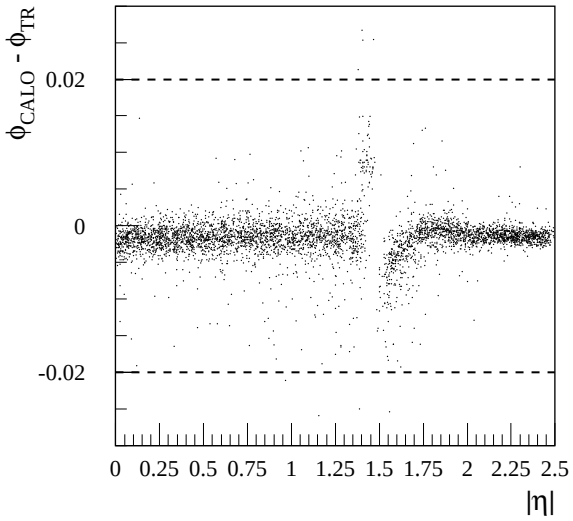

Figure 7-16 Matching in azimuth between the EM Calorimeter and ID for p_T = 20 GeV electrons.

7.2.3 Combined energy measurements

The energy measurement of an electron is degraded, both in the ID and in the Calorimeter by bremsstrahlung, leading to significant tails and to a worsening of the energy resolution. Both effects can be reduced by using the following methods, which are illustrated by results for electrons at $|\eta| = 1.1$.

Approximately 50% of electrons at $|\eta| = 1.1$ are accompanied by a conversion since there are a large number of bremsstrahlung photons (for example, on average there are 5.8 photons with $E > 10$ MeV for 20 GeV E_T electrons at $|\eta| = 1.1$). In this case the energy measured in a 3×7 window in the calorimeter is significantly reduced, as shown in Figure 7-17. Conversions can be reconstructed as described in Section 7.5.1, with an efficiency of only 1% for conversions accompanying a 10 GeV E_T electron (at $|\eta| = 1.1$), rising to 21% for a 20 GeV E_T electron and to 33% at 50 GeV. The energy in the 3×7 window when a conversion is reconstructed is also shown in Figure 7-17 – in this case, an appropriate calibration factor can be applied.

The azimuthal width of the shower, measured in the second compartment of the calorimeter, is correlated with the energy loss outside the 3×7 window. When no conversion is reconstructed, the energy in the calorimeter is taken as the energy in the window with a calibration factor depending on the width. Finally, below about 15 GeV E_T, the resolution in the ID is similar or better than in the calorimeter, in which case a weighted average of the two measurements can be made. At 10 GeV E_T and $|\eta| = 1.1$, the resolution of the calorimeter is 3.25%, the resolution of the ID is 2.63% and the combined resolution is 2.32%.

With the methods described above, the amount of the tails, defined as the fraction of events outside the interval $0.95 < E/E^{gen} < 1.05$ is reduced by about 20%, as shown in Figure 7-18.

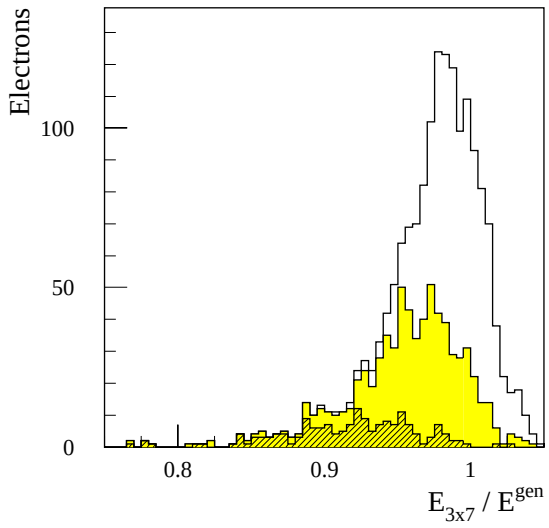

Figure 7-17 Reconstructed energy in the EM Calorimeter divided by the true energy for 20 GeV E_T electrons at $\eta = 1.1$. The histograms correspond to: electrons with reconstructed conversions (hatched), electrons with conversions which are not reconstructed (shaded), electrons without conversions (unshaded).

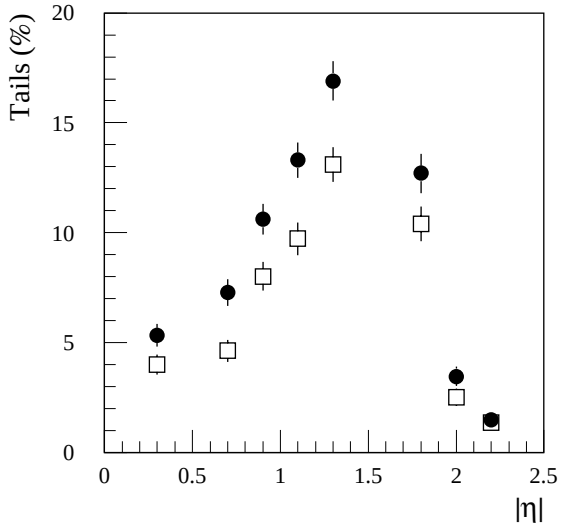

Figure 7-18 Fraction of 20 GeV E_T electrons outside $0.95 < E/E^{gen} < 1.05$ using the raw calorimeter information (black circles) and after the combined energy measurement described in the text (white squares).

7.3 Low energy electrons

7.3.1 Electron/pion separation

For low energy electrons, the trigger will be provided by something other than the electrons (for example a muon with $p_T > 6$ GeV in B physics events) and it will not be easy to identify electron candidates by an unguided search of the energy deposits in the EM Calorimeter. Instead the Inner Detector must be used to 'seed' the calorimeter clustering.

A study was made of electrons and pions in the range $1\ \text{GeV} \le p_T \le 7\ \text{GeV}$ with $|\eta| \le 2.4$. The effects of electronic noise in the EM Calorimeter were included. As the response of both subdetectors for low p_T varies quite significantly with p_T and $|\eta|$, the electron/pion separation parameters were calculated for three p_T-ranges:

$$1\ \text{GeV} \le p_T \le 2\ \text{GeV},\ 2\ \text{GeV} \le p_T \le 4\ \text{GeV} \text{ and } 4\ \text{GeV} \le p_T \le 7\ \text{GeV}$$

and five $|\eta|$-ranges:

$$0 \le |\eta| \le 0.8,\ 0.8 \le |\eta| \le 1.4,\ 1.4 \le |\eta| \le 1.8,\ 1.8 \le |\eta| \le 2.0 \text{ and } 2.0 \le |\eta| \le 2.4.$$

The following method was used to identify electrons. After track reconstruction in the ID, loose cuts were applied to all tracks: $p_T \ge 0.5$ GeV, number of precision hits ≥ 8, number of pixel hits ≥ 2, at least one associated hit in the B-layer, number of TRT straws ≥ 6, fraction of high-threshold (TR) hits in the TRT > 0.05. For selected tracks, the predicted point of impact was calculated for each of the EM Calorimeter compartments. Based on the information in the surrounding EM Calorimeter cells, the values of the EM Calorimeter and combined ID-Calorimeter separation

variables were calculated. For each of these, the probability of the track being an electron was calculated, with the set of probabilities used being determined by the p_T and pseudorapidity reconstructed in the ID. A discriminating function to distinguish between electrons and hadrons was formed as the product of the above probabilities. Some of the variables used are correlated, and although the method is valid, its treatment of these correlations is not optimal. Alternative approaches, such as neural nets, will be considered in the future. For some values of p_T and pseudorapidity, some of the variables were less discriminating and hence were not used.

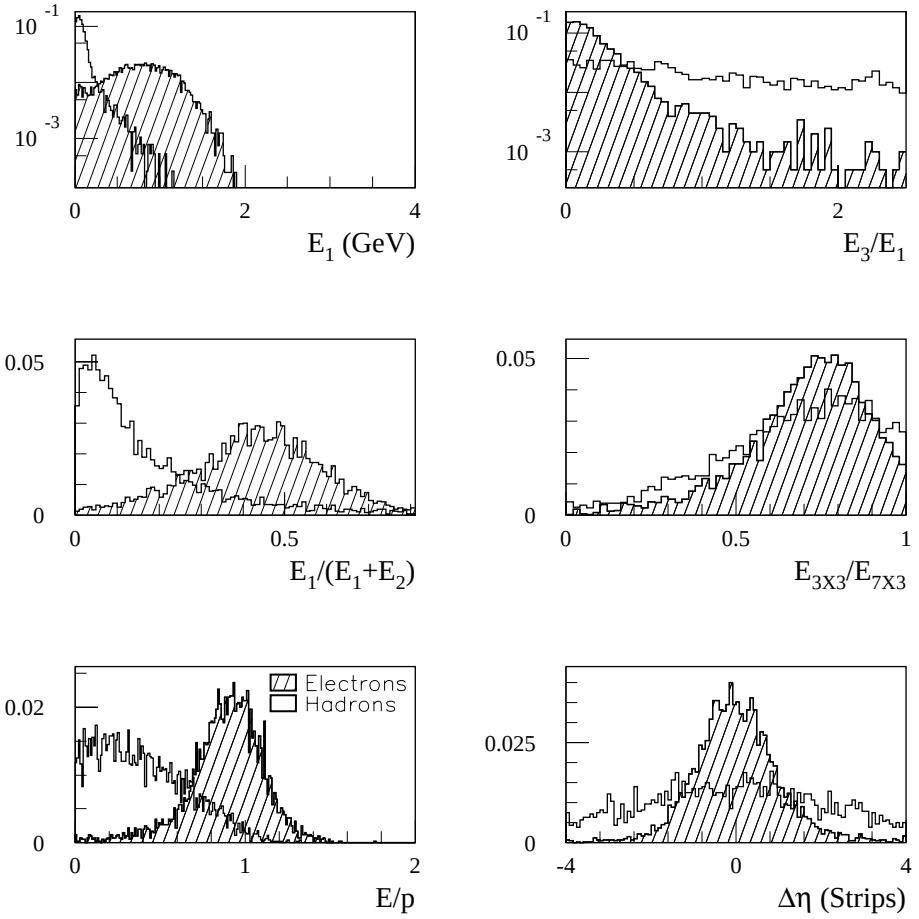

Figure 7-19 Some of the variables used to distinguish soft electrons (hatched) from hadrons (open). The histograms have been normalised to unit area. The distributions correspond to single particles with 2 GeV ≤ p_T ≤ 4 GeV and |η| < 0.8. $E_{1,2,3}$ are the energies in the first, second and third longitudinal compartments of the EM Calorimeter.

The variable used in the ID alone was: the fraction of high-threshold (TR) hits in the TRT. The variables formed in the EM Calorimeter alone were: the energy deposited in the first compartment (E_1), the ratio of energies deposited in the third and first compartments (E_3/E_1), the ratio of energies deposited in first compartment to the sum in first and second ($E_1/(E_1+E_2)$), the shower width (in pseudorapidity) in the first compartment, the ratio of energies deposited around the predicted impact point in the calorimeter in 3×3 and 3×7 clusters ($E_{3\times3}/E_{7\times3}$), and the asymmetry in the lateral shower profile measured in the first compartment by the three strips centred on the strip with the largest energy. The cracks between the barrel and the endcaps were excluded. The variables formed using the combination of the ID and the EM Calorim-

eter were: the ratio of energy measured by the EM Calorimeter to the momentum measured by the ID (*E/p*), the difference in pseudorapidity between the point of impact at the first compartment of the EM Calorimeter as predicted by ID extrapolation and as measured by the η-strips ($\Delta\eta$).

An example of the distributions for some of the more discriminating variables are shown for single particles in Figure 7-19. The distributions vary strongly with p_T and pseudorapidity; in particular, *E/p* becomes more discriminating at higher energy, which for a fixed E_T corresponds to higher pseudorapidity.

By cutting at different values of the discriminating function, different electron efficiencies can be obtained, each with a corresponding value of the rejection for single pions. The pion rejection as a function of the electron efficiency is shown in Figure 7-20 for tracks of different p_T.

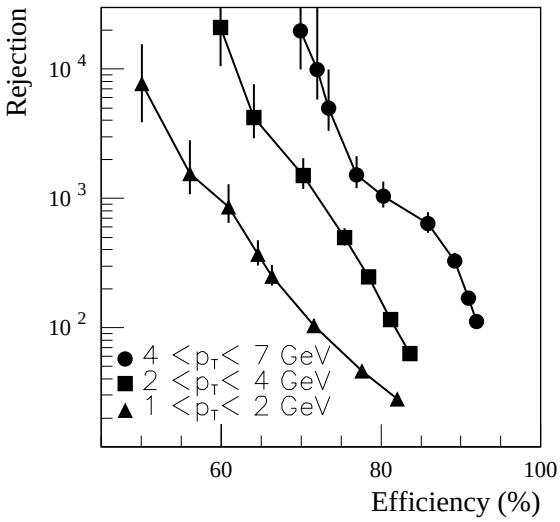

Figure 7-20 Pion rejection vs electron efficiency for single particles of different p_T.

7.3.2 Identification of low energy electrons in physics events

To identify soft electrons in complete events, it is necessary to apply the methods described above to each charged particle reconstructed in the event. In this section, the application to *B* physics events is described; the application to tagging *b*-jets is described in Chapter 10.

For this study, an inclusive $b\bar{b}$ sample was used, with the requirement of a muon with $p_T \geq 6$ GeV for triggering. A subsample of these events containing electrons with $p_T^{gen} \geq 5$ GeV were considered to be signal events, while the remainder were considered to be background. For a given event, the method outlined above was applied to each reconstructed track with $p_T > 4$ GeV and its discriminating variable was formed. For this, new probability functions were obtained from $b\bar{b}$ events.

Figure 7-21 shows the rejection against individual hadrons as a function of the electron efficiency. The electrons mostly originate from heavy flavour or τ decays, however some may come from conversions or Dalitz decays. To identify signal events containing $b \rightarrow e$ decays, the electron identification was applied to each reconstructed track in each event of the inclusive $b\bar{b}$ sample. The discriminating function was found for the best electron candidate in each event. Figure 7-22 shows the rejection of background events compared to the efficiency for identifying signal events, where the points correspond to different cuts on the value of the discriminating

function. The performance is worse than for individual particles since in the background events, there will be several tracks, any of which may be mis-identified as an electron. Further there will be electrons which do not arise from signal processes.

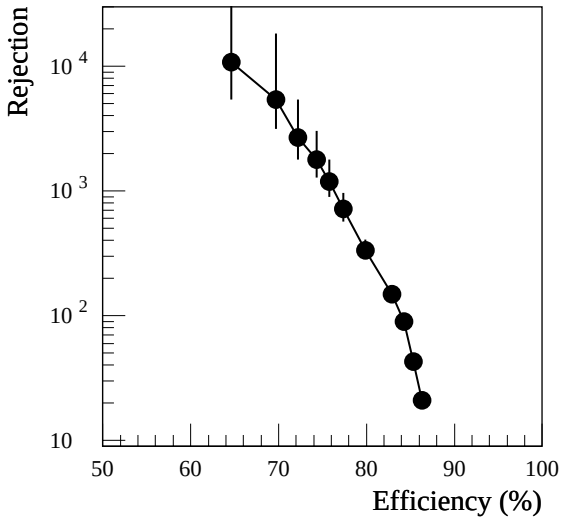

Figure 7-21 Hadron rejection vs electron efficiency for individual particles in $b\bar{b}$ events with $p_T > 4$ GeV.

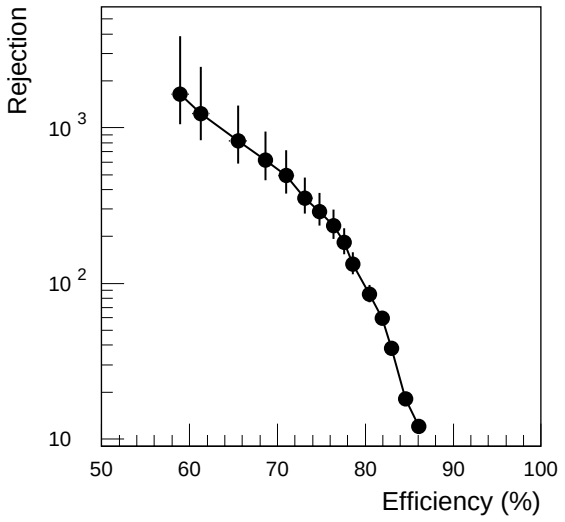

Figure 7-22 Rejection of events without $b \rightarrow e$ vs efficiency for retaining events with $b \rightarrow e$. Electrons have $p_T > 5$ GeV.

7.4 Electron/jet separation

7.4.1 Introduction

The identification of isolated electrons with $p_T \geq 20$ will be essential for physics at the LHC, including searches for leptonic decays of the Higgs boson, studies of the production and decay of W's and Z's, the extraction of clean samples of $t\bar{t}$ events for the measurement of m_t as well as electrons for E/p calibration. This section describes the inclusive electron selection and the rejection capability against QCD-jets using information from the EM Calorimeter and the Inner Detector. More details can be found in [7-2]. To obtain an inclusive electron signal, a jet rejection $O(10^5)$ is required.

To separate electrons from jets, cuts were developed which maintained reasonable electron efficiency even in the presence of pile-up at high luminosity while removing a high fraction of jet events from an inclusive jet sample. The jet sample was analysed to demonstrate that the signal electrons which it contained could be extracted from the background. In the studies reported in this section and Section 7.6, the jet rejection was normalised to the total number of jets with $E_T > 17$ GeV, smeared and reconstructed at the particle-level using ATLFAST [7-3]. This is believed to give a better reflection of the rejection which can be achieved by ATLAS and corresponds to the performance which would be observed for physical jets in the detector as opposed to partons. This normalisation results in a rejection which is a factor of three lower than would be obtained were the E_T cut applied at the parton level. The electron efficiencies have been studied for electrons at the nominal trigger thresholds for single isolated EM clusters of 20 and 30 GeV for low and high luminosity respectively.

7.4.1.1 Datasets

A high statistics sample of around 10^6 fully simulated dijet events was used [7-3]. At the parton level, each jet had $p_T > 17$ GeV and was produced within $|\eta| < 2.7$. Initial and final state radiation were simulated. At the same time, other physics processes such as prompt photon production, quark bremsstrahlung, *W*, *Z* and top production were generated with the appropriate cross-sections - the complete set of events is referred to as the 'jet sample'. These events were processed by the LVL1 trigger simulation (see Section 11.3.2) to obtain the 'electron / photon stream'. The jet rejection factor for jets having $E_T > 17$ (25) GeV was approximately 80 (90) for an electron efficiency of about 95% at low (high) luminosity. Only events with showers having a large EM component survived.

For the efficiency studies, samples of single electrons were generated with $|\eta| < 2.5$ and with fixed p_T of 20 and 30 GeV. To study the performance at high luminosity, pile-up was superimposed on the electrons and jets.

7.4.2 Analysis

The electrons and jets were first processed by the LVL1 and LVL2 trigger algorithms to select those events containing electron candidates. The events which passed the trigger were further processed by the offline reconstruction. In the following, the Calorimeter and ID selections of the offline analysis are explained; the trigger algorithms of the LVL2 trigger are explained in Section 11.4.3.

7.4.2.1 Offline calorimeter selection

Significant discrimination between electrons and jets can be achieved by the LVL2 Calorimeter Trigger. Subsequently, the offline calorimeter algorithms can refine the cuts made by the trigger as well as making additional ones.

Only EM clusters with $E_T > 17$ (25) GeV at low (high) luminosity were considered. These values correspond to the E_T threshold cut of the single object electron trigger, which are chosen to be efficient for 20 (30) GeV electrons. Figures 7-23 and 7-24 show the E_T distributions for all clusters found in the EM Calorimeter for electrons of 30 GeV and dijet events at high luminosity. The entries at low E_T correspond to clusters from low energy particles in the minimum bias events (in the case of pile-up) or particles in the jets themselves; the peaks arise from threshold cuts of around 5 GeV. It is clear that clusters from minimum bias events have low E_T and can be completely removed.

The following variables were used to distinguish high-E_T electrons from jets (more details can be found in [7-4]): the ratio of the transverse energy in the first compartment of the Hadronic Calorimeter divided by the transverse energy deposit in the EM Calorimeter, the ratio of the energy deposited in a 3×7 window divided by the energy deposited in a 7×7 window in the second compartment of the EM Calorimeter (see Figure 7-25), the shower width in pseudorapidity in the second compartment of the EM Calorimeter.

To separate the surviving jets from electrons, the very fine granularity in pseudorapidity of the first compartment was exploited by looking for substructures within a shower in pseudorapidity and by analysing the overall shower shape, using a window of $\Delta\eta \times \Delta\phi = 0.125 \times 0.2$. It was required that the fraction of EM energy in the first compartment exceeded 0.5%. The following

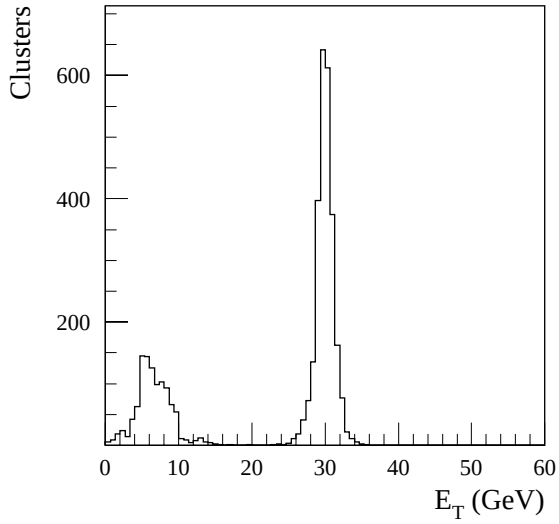

Figure 7-23 E_T distribution of all clusters in each event after LVL1 simulation in the EM Calorimeter for events with E_T = 30 GeV electrons and pile-up corresponding to 10^{34} $cm^{-2}s^{-1}$.

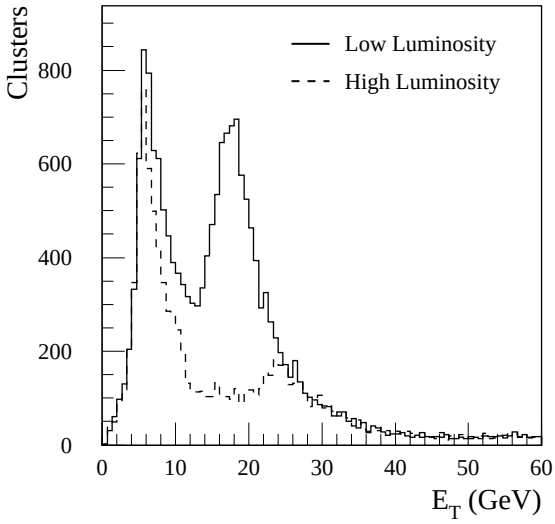

Figure 7-24 E_T distribution of all clusters in each event after LVL1 simulation in the EM Calorimeter for events with jets at both low and high luminosity.

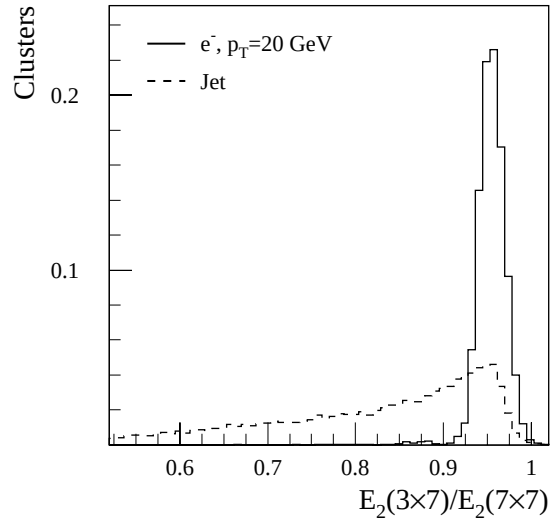

Figure 7-25 Shower shape in the second compartment of the EM Calorimeter for electrons and jets at low luminosity. Only the LVL1 Trigger was applied beforehand. The distributions are normalised to unit area.

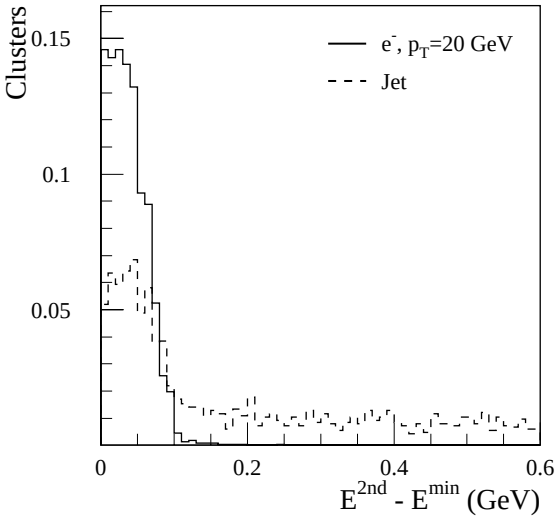

Figure 7-26 Difference between the energy found in the second maximum and the energy found in the strip with minimal value in the first compartment of the EM Calorimeter (before any cuts in first compartment). The distributions are shown for electrons and jets at low luminosity for $|\eta| < 1.37$ and are normalised to unit area.

variable was used: the difference between the energy associated with the second maximum and the energy deposited in the strip with the minimal value between the first and second maxima (see Figure 7-26.). In addition, the energy in the strip in which the second maximum was located had to exceed a value which depended linearly on the E_T of the EM cluster. Additional variables are: the shower width and the fraction of energy outside the three strips in the shower core.

The variables were optimised in several $|\eta|$ intervals to allow for varying granularities, lead thickness and material in front of the calorimeter. The quantities calculated using the first compartment can be used only in the regions $|\eta| \leq 1.37$ and $1.52 \leq |\eta| \leq 2.37$ since there are no strips in $1.4 < |\eta| < 1.5$ nor beyond $|\eta| = 2.4$. The cuts on the variables were tuned in such a way that they were more than 98% efficient for electrons after the LVL1 and LVL2 triggers.

7.4.2.2 Inner Detector selection

After the calorimeter cuts, the contamination of the inclusive signal from charged hadrons was greatly reduced and the remaining background was dominated by background from photon conversions and low multiplicity jets containing high-p_T π^0 mesons. This background was reduced further by requiring the presence of a good ID track pointing to the EM cluster and with a good energy-momentum match.

Tracks were reconstructed with xKalman (see Section 3.1.2) in a cone $\Delta\eta = \pm 0.1$, $\Delta\phi = \pm 0.1$ around the selected EM clusters, and only tracks with $p_T > 5$ GeV were kept. Where possible, the bremsstrahlung recovery procedures described in Section 7.2.1.1 were used. The reconstructed track with the highest p_T in the cone was required to satisfy the extended ID track quality cuts (see Section 3.1.3). The cuts on the pixels and impact parameter were particularly effective against photon conversions, reducing them by a factor of ~5.

7.4.2.3 Inner Detector and EM Calorimeter matching

The LVL2 trigger tends to ensure that there is an associated charged track to the EM cluster within a cone $\Delta\eta = \pm 0.1$, $\Delta\phi = \pm 0.1$. Hence the jet rejection which was achieved by the cuts in the ID was quite small, around 1.8. This was significantly improved by ensuring consistency between the EM Calorimeter and ID information. Firstly the angular matching between the track and the EM cluster was checked, allowing for the track curvature and the vertex position (see Section 7.2.2.4). It was required that $|\Delta\eta| < 0.01$ (0.02) at low (high) luminosity and $|\Delta\phi| < 0.02$. Distributions for these two variables are shown in Figure 7-27. The distributions are shown after the LVL2 trigger rather than after the ID cuts so as to increase the statistics in the plots.

Subsequently, the energies measured by the two subdetectors were compared - see Figure 7-28. At low (high) luminosity, it is required that $0.7\ (0.6) < E/p < 1.4$. The tail at low values of E/p for conversion electrons arises when one photon from a π^0 converts and the second photon was included in the EM cluster causing the track fit (incorporating the calorimeter bremsstrahlung recovery procedure) to overestimate the momentum.

7.4.2.4 Use of transition radiation in the TRT

The events which survived the selection procedure described so far consisted mainly of signal electrons. At low luminosity, where the E_T cut is at 17 GeV, 80% of the events came from heavy flavour and 20% from W's and Z's; at high luminosity, the E_T cut rises to 25 GeV and the fractions became 20% and 80% respectively. The contamination of the jet sample arising from the mis-identification of charged hadron backgrounds was 30% (40%) of the jets at low (high) luminosity. The contamination from electrons coming from photon conversions was greatly reduced by the previous cuts.

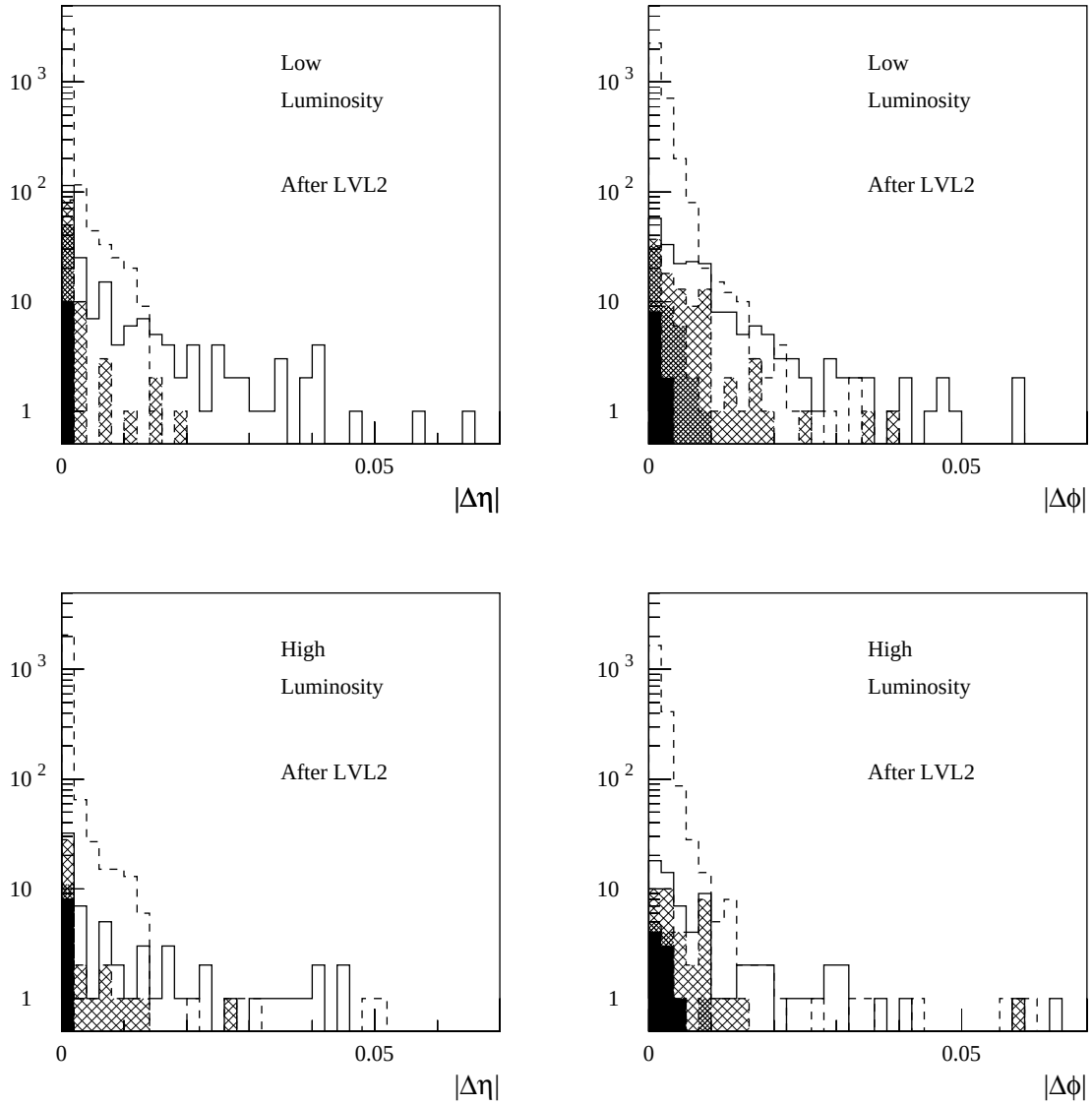

Figure 7-27 Angular matching between charged tracks and EM clusters in pseudorapidity and azimuth for electrons (dashed) and jets. For the 'jet' sample, various components are shown: electrons from *W*'s and *Z*'s (black), electrons from heavy flavour (dense hatch), conversions (light hatch) and hadrons (open). The normalisation between the single electrons and the jet sample is arbitrary.

To reduce further the charged hadron contamination, candidate electrons were required to pass the loose transition radiation cuts described in Section 3.4.1. These cuts retained 90% of the electrons and, with the available jet statistics, reduced the hadrons from 17 (6) events to 0 (1) at low (high) luminosity, consistent with expectations.

7.4.3 Summary of results

Summaries of the electron efficiencies and corresponding jet rejections resulting from the succession of cuts applied and in different pseudorapidity intervals are given in Tables 7-1 and 7-2 respectively. The electron efficiencies are determined from the high-statistics electron samples, while the jet rejection is calculated from the reductions in the jet sample but with the signal electrons explicitly excluded. To normalise the jet rejection, only jets with $E_T > 17$ (25) GeV have

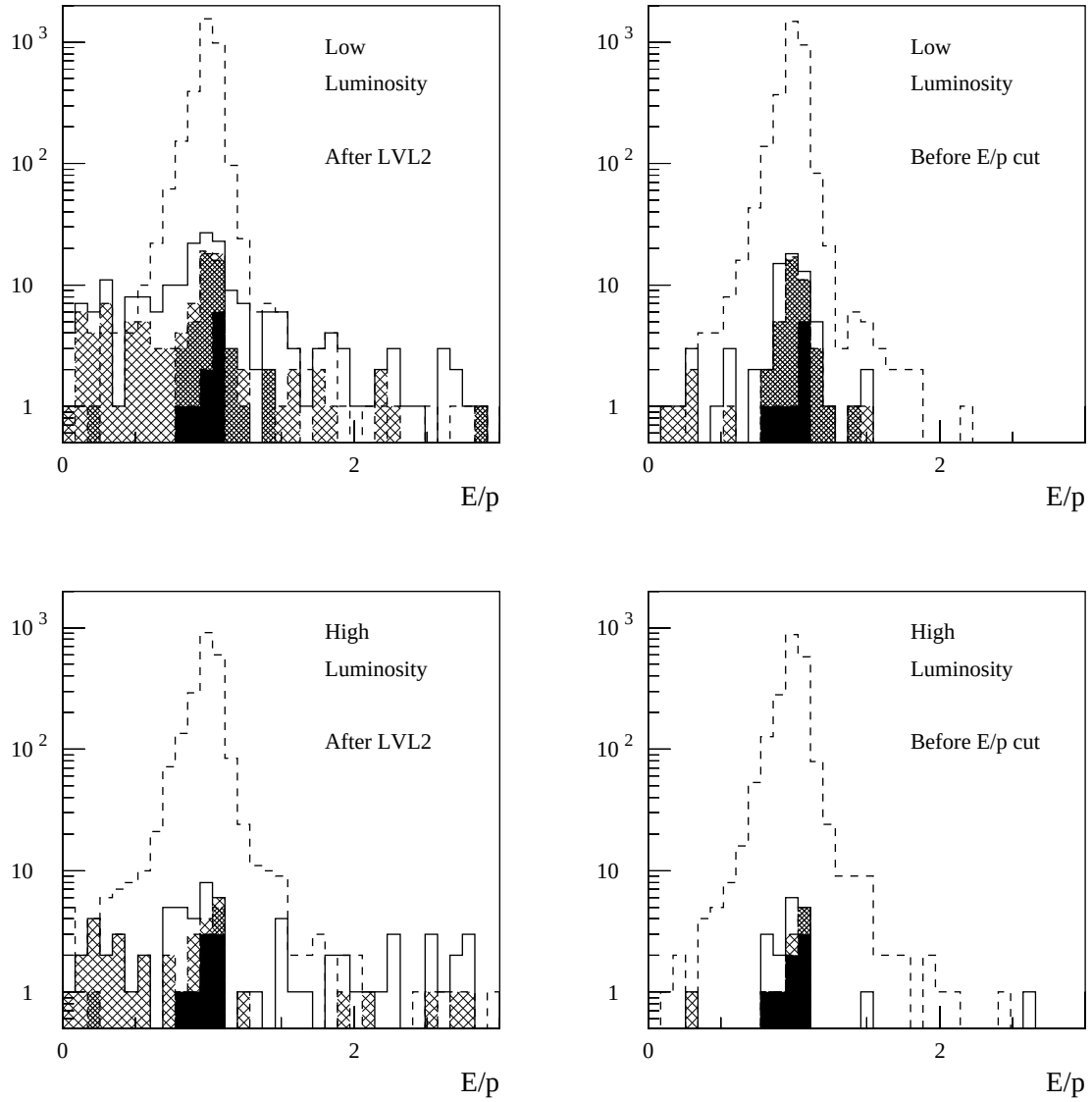

Figure 7-28 Ratio between energy of EM clusters to momentum of reconstructed charged tracks for electrons (dashed) and jets. For the 'jet' sample, various components are shown: electrons from *W*'s and *Z*' s (black), electrons from heavy flavour (dense hatch), conversions (light hatch) and hadrons (open). The normalisation between the single electrons and the jet sample is arbitrary.

been considered at low (high) luminosity. The final jet rejections correspond to 1 (2) events at low (high) luminosity and the values in Table 7-1 correspond to 90% confidence limits calculated according to the prescription in [7-5]. In Figure 7-29, the E_T distributions of candidates in the jet sample are shown at low and high luminosity at various stage of the offline analysis.

With the cuts described in this section, it was possible to achieve an overall electron efficiency for p_T = 20 GeV (30 GeV) of 68.6% (72.7%) at low luminosity. The addition of pile-up decreased the efficiency for the 30 GeV electrons down to 67.5%, which is comparable to what was achieved at low luminosity for 20 GeV electrons. A corresponding jet rejection of the order of 10^5 was obtained at both low and high luminosity. For such a large rejection factor, the results will be sensitive to the details of the fragmentation model at a level which is not well tested. Hence there may be considerable systematic uncertainties. Compared to the tabulated results (in particular, Tables 6-2 and 6-4) in the ID TDR [7], the electron efficiency has fallen by 20%

Table 7-1 Effect of different sets of cuts on electron efficiencies (p_T = 20 and 30 GeV) and jet rejections (E_T > 17 GeV and |η| < 2.5). The cuts are described in more detail in the text. The numbers shown are the effect of the cumulative cuts, with the relative changes (percent or absolute numbers) shown in brackets.

Cuts	Low luminosity						High luminosity			
	Eff e_{20} (%)		Eff e_{30} (%)		Rej jets (10^3)		Eff e_{30} (%)		Rej jets (10^3)	
LVL1	94.0		99.0		0.08		96.1		0.09	
LVL2 Calo	90.5	(96.3)	96.9	(97.8)	0.39	(4.9)	92.1	(95.6)	0.48	(5.2)
LVL2 ID	82.5	(91.1)	87.9	(90.7)	3.5	(8.9)	82.5	(89.5)	3.7	(7.8)
Offline Calo	80.9	(98.1)	86.8	(98.6)	9.8	(2.8)	81.1	(98.3)	8.4	(2.2)
Offline ID	77.4	(93.8)	83.0	(94.5)	16.8	(1.7)	77.2	(93.6)	22.7	(2.7)
Matching	75.4	(97.5)	79.5	(95.7)	40	(2.4)	75.3	(97.4)	35.8	(1.6)
TR	68.5	(90.8)	72.7	(91.4)	>150		67.5	(89.7)	>45	

mainly because of the explicit application of the transition radiation (TR) cuts (loss of 10%), the simulation of the trigger as well as tighter Inner Detector cuts (number of TRT and pixel hits). The trigger losses can be broken down as follows: 2.3% (5.6%) due to the ID cuts in LVL2, 1.5% (1.5%) due to the calorimeter cuts in LVL2 and 2% (3%) in LVL1 at low (high) luminosity. At the same time, the rejection has increased by a factor 50 mainly because of the TR cuts and the improved calorimeter and ID cuts.

The selection procedure outlined above leads to a signal (inclusive electrons) to background (charged hadrons and conversions) ratio of more than 20 (5) for low (high) luminosity, although large uncertainties remain on the cross-sections for the different processes. The electron efficiency was cross-checked by considering the signal electrons in the inclusive jet sample. However, since the fraction of events with electrons in the sample was very small, the statistical errors are large. For electrons coming from *W/Z* decays, the efficiency is $(54 \pm 13)\%$ ($(60 \pm 15)\%$) and for those coming from *b* and *c* semi-leptonic decays, it is $(14 \pm 2.5)\%$ ($(3.4 \pm 2.4)\%$) for low (high) luminosity - the errors are from Monte Carlo statistics. With the statistics used, it was not meaningful to analyse the background events because there were so few. At low luminosity, all that remained was one conversion; at high luminosity, there was one conversion and one mis-identified hadron.

7.5 Photon measurements

The most demanding requirements for excellent photon measurement and identification arise from the search for a possible Standard Model Higgs boson in the mass range from the LEP limit to 130 GeV. In this mass region, the most promising discovery channel for the Higgs boson is its rare decay to two photons. The signal ($\sigma \sim 50$ fb) has to be observed above large backgrounds and the observed width will be dominated by the energy resolution. Photon reconstruction is mainly based on the information from the EM Calorimeter and is described extensively in Chapter 4. Because of the significant amount of material in front of the calorimeters, many of the photons are converted. Since the $H \rightarrow \gamma\gamma$ signal is small, it is essential to ensure high efficiency, and consequently to recover the conversions. The Inner Detector helps to reconstruct these converted photons and to veto tracks around an EM cluster. The available information can improve the energy measurement as well as the photon identification power.

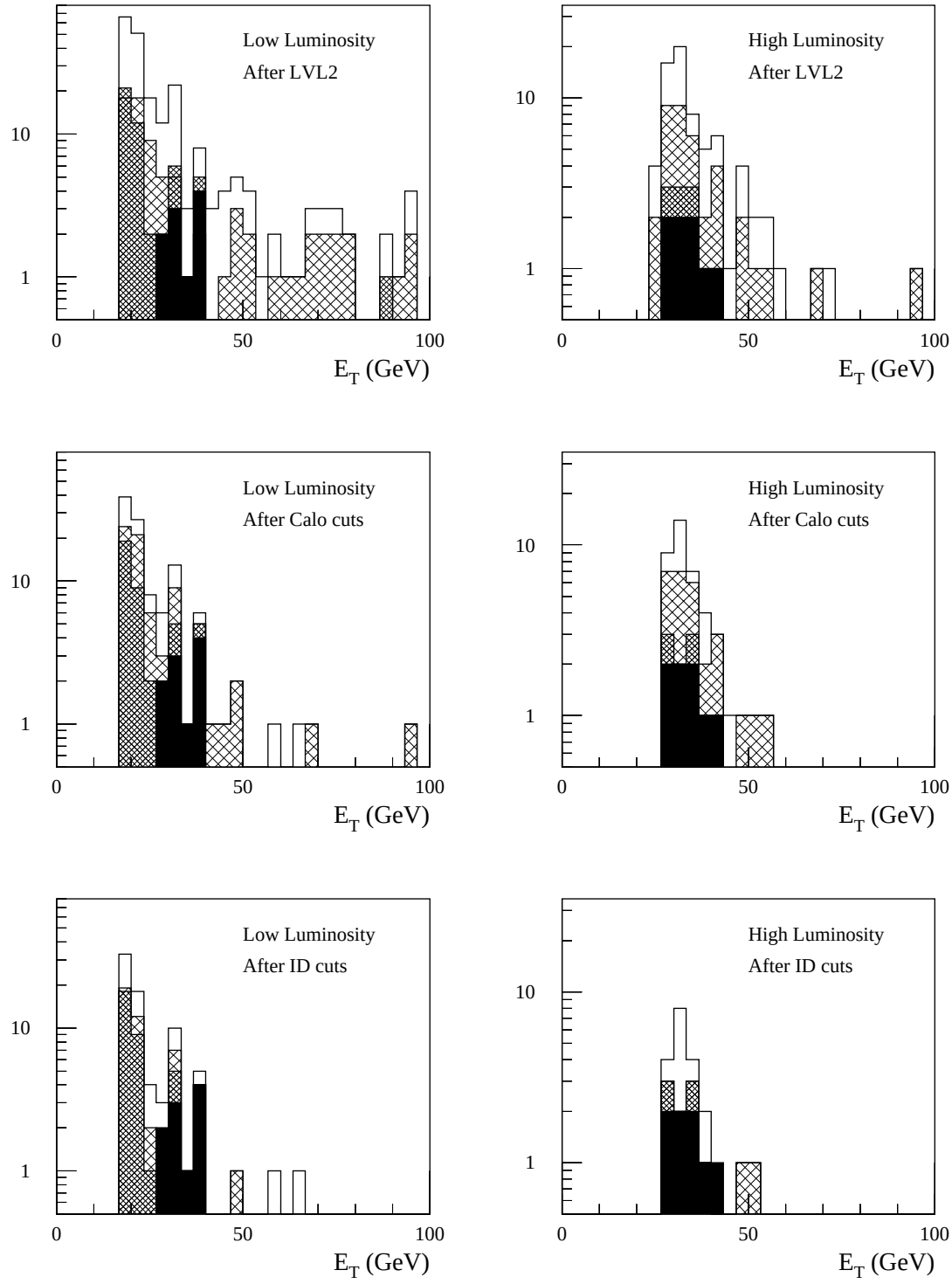

Figure 7-29 E_T distribution for the jet sample at various stages of the analysis both at low and high luminosity. For the 'jet' sample, various components are shown: electrons from *W*'s and *Z*'s (black), electrons from heavy flavour (dark hatch), conversions (light hatch) and hadrons (open).

Table 7-2 Electron efficiencies (p_T = 20 and 30 GeV) after all cuts as a function of pseudorapidity.

Pseudorapidity	Low Luminosity		High Luminosity
	Eff e_{20} (%)	Eff e_{30} (%)	Eff e_{30} (%)
0.0 - 0.7	74.7 ± 1.3	75.0 ± 1.4	70.6 ± 1.6
0.7 - 1.37	68.0 ± 1.4	72.6 ± 1.4	68.4 ± 1.7
1.37 - 1.52	45.3 ± 3.3	49.0 ± 3.4	40.4 ± 3.9
1.52 - 2.0	64.3 ± 1.7	75.2 ± 1.7	65.1 ± 2.1
2.0 - 2.5	71.6 ± 1.6	74.3 ± 1.7	72.8 ± 2.1

Around 30% of all photons convert in the material of the ID cavity (R < 115 cm). Figure 7-30 shows that around 75% of these conversions occur in the volume (R < 80 cm, $|z|$ < 280 cm) in which they can be efficiently identified. Depending on the pseudorapidity, the conversion fraction within this volume varies between 15% and 30%. Conversions occurring outside this region are less harmful because the electrons do not bend much in the azimuthal direction before entering the EM Calorimeter, and hence look more like unconverted photons.

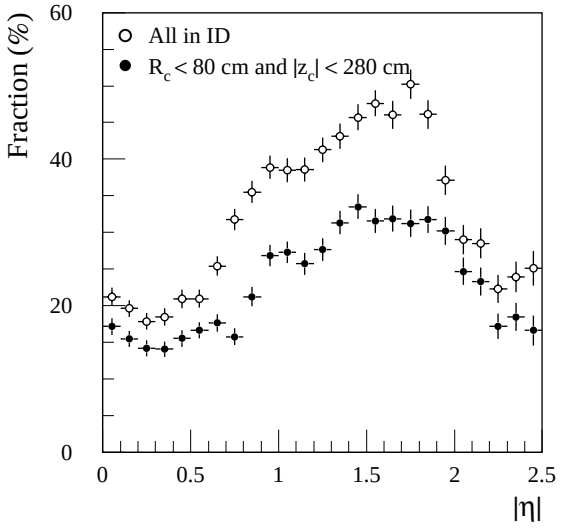

Figure 7-30 Fraction of photons converted in the ID cavity (open symbols) and in the region in which conversions can be efficiently identified (closed symbols) as a function of pseudorapidity.

7.5.1 Conversion reconstruction

7.5.1.1 Methods

Conversions are found by the program xConver which combines pairs of oppositely charged tracks [7-7]. For early conversions (R < 40 cm), both tracks can be reconstructed by xKalman (see Section 3.1.2), provided the minimum number of silicon hits on a track is relaxed to 4 (corresponding to the two outmost SCT layers). For later conversions (R > 40 cm), xKalman fails to reconstruct the tracks because insufficient silicon hits are available and because the histogramming method used to find the TRT track seed fails.

To maintain efficiency for later conversions which take place in the TRT, an algorithm, xHouRec [7-7], was written specifically to find tracks from conversions. This histogramming algorithm generalises the xKalman histogramming by scanning for tracks in the (ϕ, κ, R_c) space (xKalman histogramming assumes R_c = 0), where ϕ is the azimuthal angle at the point of closest approach to x = 0, y = 0; κ is the signed curvature; and R_c is the radius of the conversion. The track candidate is assumed to point to the interaction region from the radius R_c. In the absence of silicon hits, there is no information on the track in pseudorapidity.

A search is made by xConver for pairs of oppositely charged tracks with $p_T > 0.5$ GeV reconstructed from either algorithm (xKalman or xHouRec). A preselection is made on the basis of the separation of the tracks in the bending plane at the radius of their innermost hits. A χ^2 fit is performed using the parameters of the two tracks with the constraints of a common vertex in 3D, a zero opening angle between the tracks, and the pointing of the reconstructed photon to the beam-line.

In case more than one conversion is reconstructed in the search region, the combination with highest photon p_T is chosen. A conversion identified by xHouRec tracks is only considered if no conversion is found using tracks reconstructed by xKalman.

7.5.1.2 Reconstruction efficiency

Figure 7-31 shows that the reconstructed momentum of a converted photon is measured better for those photons which convert early ($R < 40$ cm) as opposed to the later conversions ($R > 40$ cm). The inclusion of hits in the silicon detectors and the larger track length in the magnetic field improve the p_T resolution significantly. The low energy tails in the distribution of p_T / p_T^{gen} are due to instances of hard bremsstrahlung.

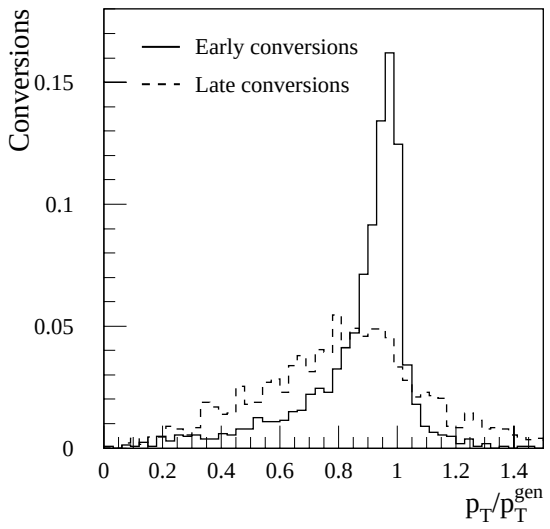

Figure 7-31 Reconstructed transverse momentum of conversions divided by the true transverse momentum for photons from Higgs events for conversions in which the two tracks are found by xKalman (solid) and by xHouRec (dashed). The distributions are normalised to unit area.

The conversion reconstruction was studied for photons from $H \rightarrow \gamma\gamma$ decays with $m_H = 100$ GeV. The overall reconstruction efficiency at low luminosity was $(86.4 \pm 0.4)\%$ per photon after the kinematical cuts ($|\eta| < 2.5$, $E_T(\gamma_1) > 40$ GeV, $E_T(\gamma_2) > 25$ GeV). This efficiency was normalised to the number of converted photons with a conversion radius $R_c < 80$ cm and a z-component of $|z_c| < 280$ cm at the generator level. Figure 7-32 demonstrates that the dependence on the conversion radius is small. The figure also shows that at low radii, conversions can be identified by combining xKalman tracks and for higher radii, by combining xHouRec tracks. In total, around 60% of all identified conversions were reconstructed by xHouRec tracks. The reconstruction efficiency was fairly independent of pseudorapidity (see Figure 7-33) with the exception of the transition region between the barrel and end-cap TRT, where xHouRec was inefficient.

At high luminosity, fake conversions arise from combinatorial background. The fake rate is pseudorapidity dependent and below 1% [7-7]. These fake conversions typically have a p_T of 1 or 2 GeV, which is much less than the p_T typical of a converted photon from a signal event and hence, the fakes can be suppressed easily.

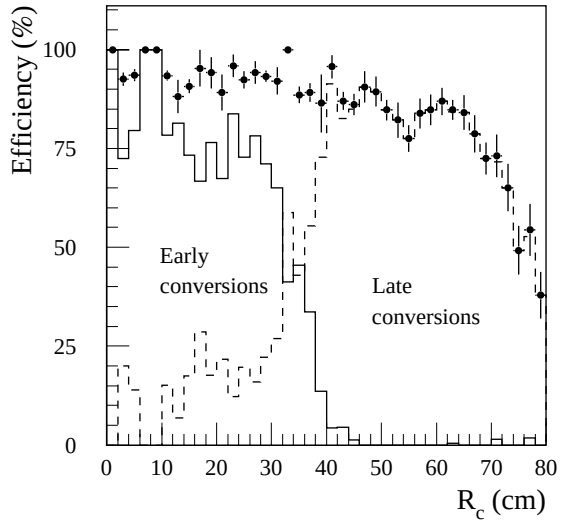

Figure 7-32 Efficiency (solid circles) for reconstructing converted photons from Higgs decays as a function of the conversion radius R_c. The contributions of conversions identified by xKalman tracks (early conversions) and by xHouRec tracks (late conversions) are shown separately.

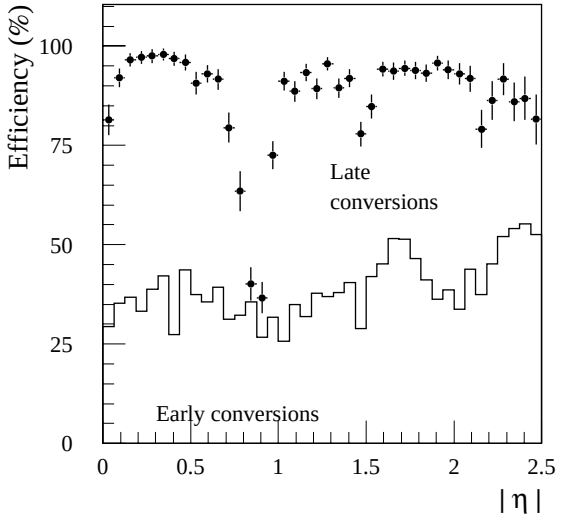

Figure 7-33 Efficiency (solid circles) for reconstructing converted photons from Higgs decays as a function of pseudorapidity. The contributions of conversions identified by xKalman tracks (early conversions - lower band) and by xHouRec tracks (late conversions - upper band) are shown separately.

7.5.2 Combined energy measurement using the EM Calorimeter and ID

Figure 7-34 shows that the energy deposited by a photon in a 3×5 window of the EM Calorimeter exhibits large tails on the low energy side because of conversions occurring in the ID. The size of the tails, defined as the fraction of events outside 0.95–1.05 of the true energy, is shown in Figure 7-35 for 20 GeV E_T photons. For unconverted photons, the tails are at the level of a few percent, apart from the crack regions where the energy resolution degrades. For converted photons, the amount of tails is more than 30% for $|\eta| < 1.8$, decreasing at higher rapidities as the ID material and the integrated magnetic field decrease.

In the Calorimeter Performance TDR [7-8], the tails were reduced by using a 3×7 window for converted photons, with the conversion being identified from the Monte Carlo truth information and corrected by the conversion finding efficiency. In the study presented here, full simulation and reconstruction of the ID and EM Calorimeter were used.

Local energy maxima were searched for in the EM Calorimeter, with $E_T > 2$ GeV. With this energy threshold, $\sim 6\times10^{-3}$ clusters per event due to electronic noise and pile-up in the EM Calorimeter were found in a window of $\Delta\eta\times\Delta\phi = 0.1\times0.1$ at high luminosity. The probability to lose a photon was less than 0.1% for $E_T > 10$ GeV and the probability to reconstruct two clusters for a single photon was maximal at $E_T \sim 10$ GeV, $|\eta| = 1.7$, and was about 4%.

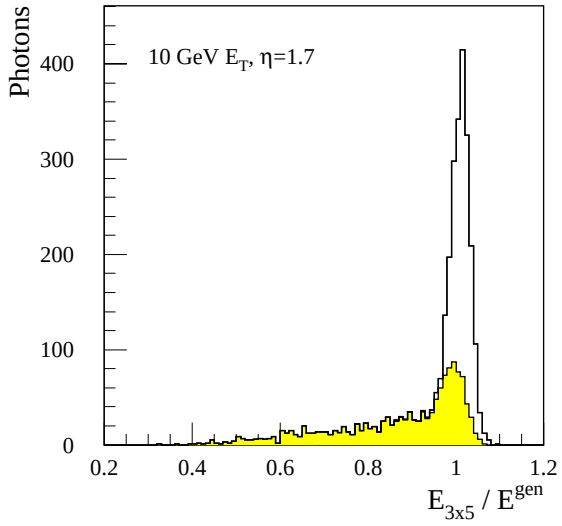

Figure 7-34 Energy in a 3×5 window divided by the true energy for all photons (histogram) and for converted photons (grey histogram).

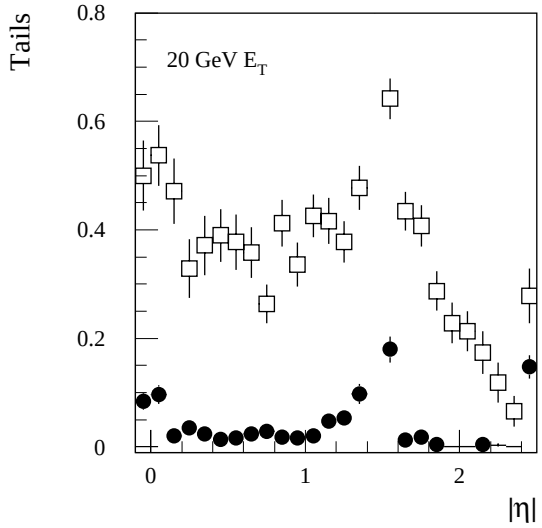

Figure 7-35 Fraction of tails for 20 GeV E_T photons, as a function of pseudorapidity, for non converted photons (black dots) and converted ones (open squares).

When a conversion was found in the ID, a 3×7 window was used in the EM Calorimeter. Figure 7-36 shows the fraction of energy reconstructed in such a window (for converted photons), as a function of the conversion radius and the transverse energy of the photon. A calibration which depends on E_T and R_{conv} was applied (using reconstructed quantities), and which, to first order, was independent of $|\eta|$. In addition, the transverse momentum of the conversion measured in the ID was combined with the corrected calorimeter energy, leading to a reduction in the tails and an improved energy resolution for photons below 20 GeV E_T.

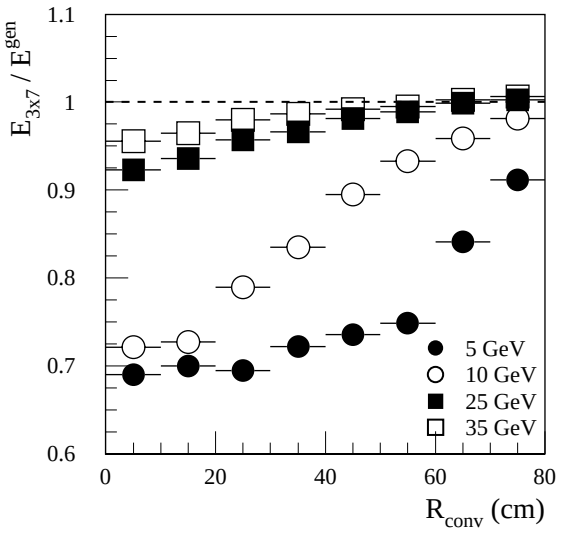

Figure 7-36 Energy in a 3×7 window versus conversion radius, for photons with a reconstructed conversion.

Figure 7-37 shows how the energy distribution was improved for 10 GeV E_T converted photons at $|\eta| = 1.7$ by using this algorithm. The distribution was well centred at 1, and the fraction of events outside 0.95–1.05 was reduced by 20% for $|\eta| < 1.8$ and $E_T < 35$ GeV. As shown in Figure 7-38, the energy resolution is improved by almost a factor two in the absence of electronic noise or pile-up. When they were included, there was still an improvement in the energy resolution, even at low energies, but it was quite small.

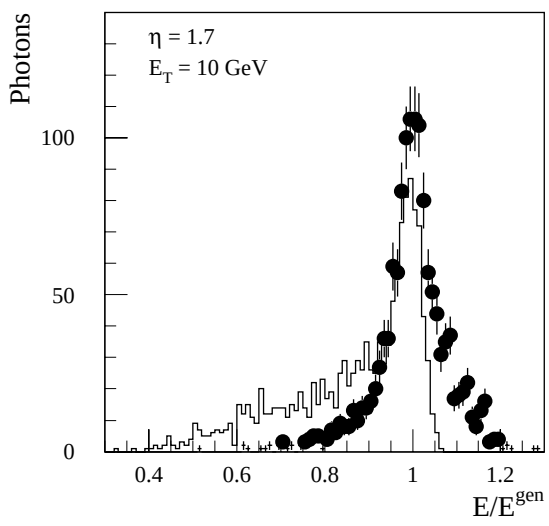

Figure 7-37 Energy distribution for converted photons using a 3×5 window (histogram) and using the EM Calorimeter and ID information (dots).

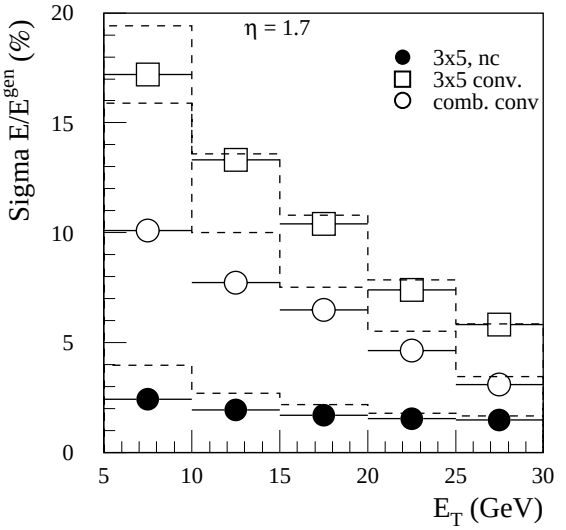

Figure 7-38 Energy resolution for unconverted photons (black dots), converted photons using a 3×5 window (open squares) and converted photons combining the EM Calorimeter and ID information (open circles). The dashed histograms show the values when electronic noise and pile-up in the EM Calorimeter at high luminosity were included.

7.6 Photon/jet separation

7.6.1 Introduction

In this section, the photon/jet separation is presented over the full pseudorapidity range used for precision physics ($|\eta| \leq 1.37$ and $1.52 \leq |\eta| \leq 2.47$) both at low and high luminosity. The separation relies mainly on the analysis of the shower shape in the EM Calorimeter. Some further optimisation can be achieved by reconstructing converted photons in the ID (see Section 7.5.1) and using a track veto. Further information can be found in reference [7-4].

The jet sample ($p_T > 17$ GeV) described in Section 7.4.1.1 was used. In addition, a similar jet sample of 10^6 dijet events with parton $p_T > 35$ GeV was used. After the application of the LVL1 trigger simulation, the total jet rejection was approximately 80, while the photon efficiency was nearly 100%. In this study, the performance for single objects (photons or jets) was considered. The LVL1 simulation was based on the EM20I object (see Section 11.7.3) associated with a nominal 20 GeV threshold. At high luminosity, the nominal single isolated EM cluster threshold is 30 GeV. However, $H \rightarrow \gamma\gamma$ events may still be selected with the double cluster trigger 2×EM20I. Hence for both low and high luminosity studies, the nominal 20 GeV threshold was used for LVL1 calorimeter trigger. To determine the photon efficiencies, a sample of 10^4 $H \rightarrow \gamma\gamma$ events ($|\eta| < 2.5$, $E_T(\gamma_1) > 40$ GeV, $E_T(\gamma_2) > 25$ GeV) was used.

7.6.2 Analysis

Photons can be identified by analysing the leakage of EM showers into the Hadronic Calorimeter and the shower shape seen in the first and second compartments of the EM Calorimeter. This analysis can be performed separately for converted and unconverted photons. In this analysis, the cuts were designed to achieve an 80% photon efficiency, independent of E_T and pseudorapidity.

7.6.2.1 Offline calorimeter selection

The quantities used for photon identification were the same as used for electron identification (see Section 7.4.2.1). Energetic photons tend to shower later than a jet consisting of several photons, where there is a higher chance that one of the photons will initiate an early shower. To be able to use cuts on the shower profile within the first compartment, it was required that the fraction of EM energy in this compartment exceeded 0.005. Clusters failing this cut were classified as photons.

In addition to the variables used for electron/jet separation, the shower shape in the azimuthal direction in the second compartment of the calorimeter helps to distinguish between photons and jets. Figure 7-39 shows the ratio of energy deposited in a 3×3 window divided by the energy deposited in a 3×7 window in the second compartment $E_2(3\times3)/E_2(3\times7)$. The isolation in the azimuthal direction was worse than was seen in pseudorapidity because the electrons from a conversion bend in the magnetic field in the ID volume.

The cuts in the EM Calorimeter used for photon/jet separation were optimised, using the ID information to identify converted photons (see Section 7.5.1). In particular, this led to improvements associated with the cuts on the ratio $E_2(3\times3)/E_2(3\times7)$ measured in the second compartment and on the corrected width in the first compartment using the three central strips.

7.6.2.2 Offline Inner Detector selection

To ensure that reconstructed conversions were consistent with coming from single photons, the momentum of the reconstructed conversion in the ID was compared with the energy measured in the EM Calorimeter. This was particularly useful for removing π^0 decays where one of the photons had converted but the second had not. For reconstructed conversions at low luminosity, it was required that $p/E > 0.6$ (0.4) for early (late) conversions. These cuts were not applied at high luminosity since the proximity to signal photons of low energy background or fake conversions would cause a significant efficiency loss. The p/E distribution is shown in Figure 7-40 for low luminosity. The photons which were lost arose mainly from conversions in which one or both of the electrons underwent bremsstrahlung causing the tracks to be poorly reconstructed. Since events containing these photons tend to end up in the tails of distributions, if they are not removed at this stage, they are likely to removed by subsequent analysis cuts.

To achieve a further improvement in the photon/jet separation, a track veto was applied. In the case where no conversion was identified satisfying the cut on p/E, an EM cluster was retained provided there was no track associated ($|\Delta\eta| < 0.1$, $|\Delta\phi| < 0.2$) which passed the ID quality cuts and had $p_T > 5$ GeV. This p_T threshold ensured that even at high luminosity, a high photon efficiency was maintained.

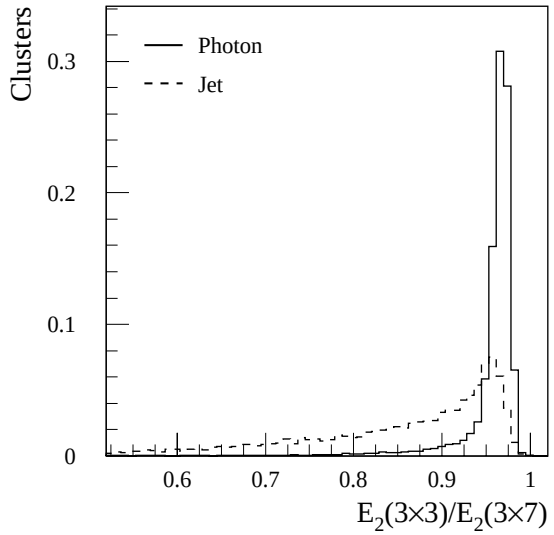

Figure 7-39 Distribution showing the azimuthal shape for photons from $H \rightarrow \gamma\gamma$ and jets. The distributions are normalised to unit area.

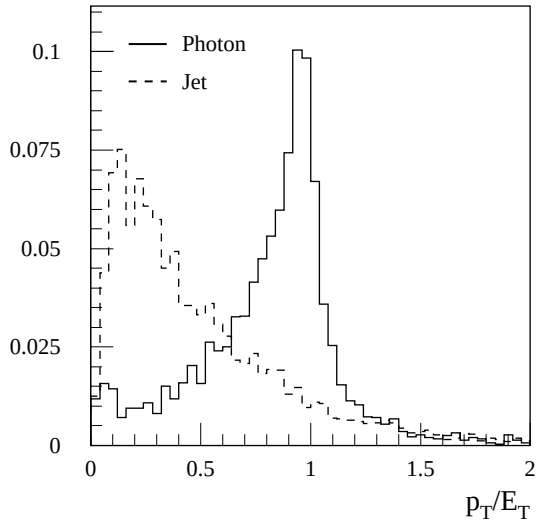

Figure 7-40 Ratio of the p_T of a conversion reconstructed in the ID to the E_T measured in the EM Calorimeter for converted photons from $H \rightarrow \gamma\gamma$ and for jets. The distributions are normalised to unit area.

7.6.3 Results

The jet rejection was tuned for an efficiency of ~80% at all E_T's for photons from $H \rightarrow \gamma\gamma$ events. Photon identification is based mainly on calorimeter information, hence tighter constraints for the calorimeter quantities were applied than those used for electron/jet separation. As was discussed for the electron/jet separation, these variables are pseudorapidity dependent and were optimised in the same pseudorapidity intervals. The transition region between the barrel and end-cap calorimeters and the region $|\eta| > 2.47$ were excluded (see Section 7.4.2.1).

Table 7-3 Effect of different sets of cuts on photon efficiencies (from $H \rightarrow \gamma\gamma$, with $m_H = 100$ GeV, $|\eta| < 2.5$, $E_T(\gamma_1) > 40$ GeV, $E_T(\gamma_2) > 25$ GeV) and jet rejections ($E_T > 17$ GeV and $|\eta| < 2.5$). The cuts are described in more detail in the text. The numbers shown are the effect of the cumulative cuts, with the relative changes (percent or absolute numbers) shown in brackets. The transition between the barrel and the end-cap is excluded.

Cuts	**Low luminosity**						**High luminosity**			
	Eff γ (%)		**Rej jets $E_T \approx 20$ GeV**		**Rej jets $E_T \approx 40$ GeV**		**Eff γ (%)**		**Rej jets $E_T \approx 20$ GeV**	
LVL1	100.0		76		210		99.2		74	
Had Calo	95.7	(95.7)	130	(1.8)	430	(2.0)	94.9	(95.7)	110	(1.5)
2nd Compart.	90.2	(94.3)	390	(2.9)	1220	(2.8)	89.7	(94.5)	300	(2.7)
1st Compart.	85.7	(95.0)	1050	(2.7)	2700	(2.2)	84.0	(93.6)	840	(2.8)
p/E for Conv. γ	84.4	(98.5)	1170	(1.1)	2700	(1.0)				
Track veto	83.0	(98.3)	1270	(1.1)	2900	(1.1)	83.1	(98.9)	910	(1.1)

The jet rejection after the different cuts are shown in Table 7-3 for low and high luminosity. The rejections are normalised to the total number of jets with $E_T > 17$ GeV reconstructed at particle level using the fast simulation program ATLFAST [7-9]. The variables used for the calorimeter cuts are correlated, and hence the actual rejections obtained with each cut depend on the order of the cuts. The jet rejections as a function of the jet E_T are shown in Figure 7-41. A total jet rejection of 1270 ± 80 (910 ± 50) is achieved at low (high) luminosity for jets with E_T around 20 GeV - the errors are from Monte Carlo statistics. For jets with E_T around 40 GeV, the rejection is 2900 ± 300 (3100 ± 800). These rejections are a factor of ~2 less than reported in [7-8] due to the normalisation using ATLFAST - see Section 7.4.1. The corresponding photon efficiencies as a function of rapidity for $H \rightarrow \gamma\gamma$ with m_H = 100 GeV are shown in Figures 7-42 and 7-43. The average efficiencies are (83.0 ± 0.3)% ((83.1 ± 0.6)%) at low (high) luminosity. The cuts applied tended to reject more converted than unconverted photons, which is due mainly to the cut on the isolation in azimuth in the second compartment and the corrected width in the first compartment. After all the cuts, the composition of the jet sample was: 55% (31%) photons from π^0, η, η', ω (dominated by isolated π^0's), 18% (33%) photons from quark bremsstrahlung, 6% (5%) from neutral hadrons and 21% (31%) direct photons (which should be considered as a signal) for E_T around 20 GeV (40 GeV). More details of the breakdown after each set of cuts can be found in reference [7-4].

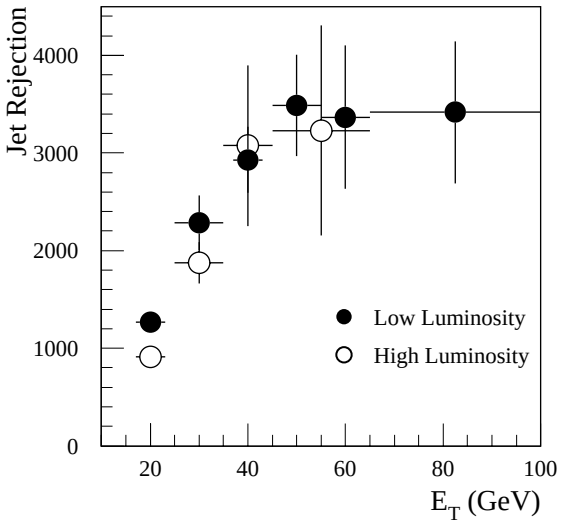

Figure 7-41 Jet rejection after photon selection cuts as a function of jet E_T for low and high luminosity.

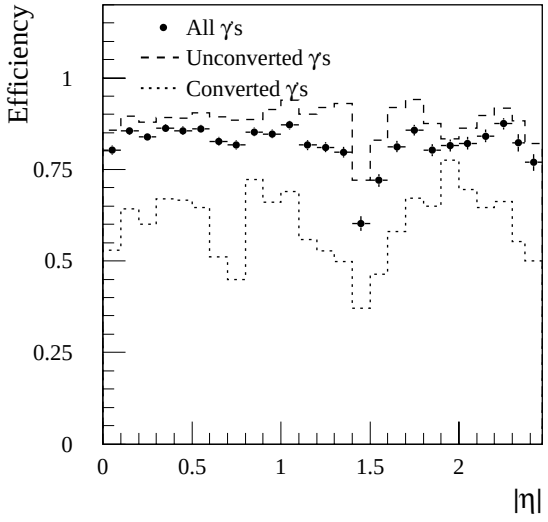

Figure 7-42 Photon efficiencies for photons from $H \rightarrow \gamma\gamma$ with m_H = 100 GeV at low luminosity as a function of pseudorapidity. The photon efficiencies are shown for unconverted (dashed line) and converted photons (dotted line). Events in the crack ($1.37 < |\eta| < 1.52$) are not used.

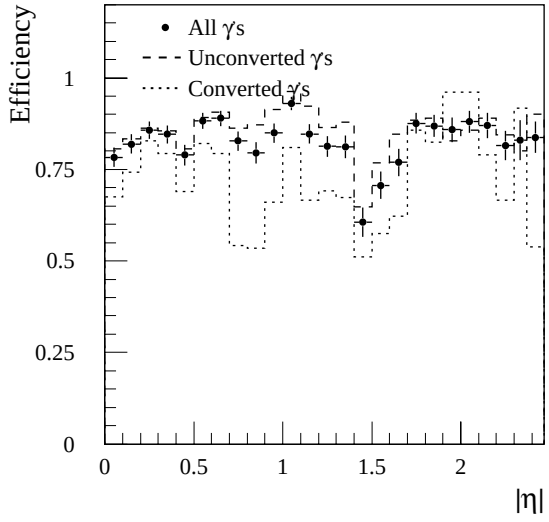

Figure 7-43 Photon efficiencies for photons from $H \rightarrow \gamma\gamma$ with m_H = 100 GeV at high luminosity as a function of pseudorapidity. The photon efficiencies are shown for unconverted (dashed line) and converted photons (dotted line). Events in the crack ($1.37 < |\eta| < 1.52$) are not used.

If the LVL2 photon trigger (see Section 11.4.3) was applied in addition to the offline analysis, only 0.06% (0.3%) of the Higgs events which otherwise would be accepted by the offline analysis were rejected by the trigger at low (high) luminosity. The photon identification variables used in the trigger correspond to a subset of those used in the offline analysis, but with much looser cuts and slightly different definitions for the clusters.

7.7 Photon/electron separation

Photon / electron separation for $E_T \sim 40$ GeV is essential for the $H \rightarrow \gamma\gamma$ search when the Higgs boson mass is close to the Z mass (this is now close to being ruled out for a Standard Model Higgs). If electrons are mis-identified as photons, the large Z cross-section at resonance can result in a significant background to the Higgs boson. To enable the $\gamma\gamma$ signal to be seen, an electron rejection of ≥500 is needed to reduce the background to 10% of the signal. An electron may be mis-identified as a photon if the electron track is not reconstructed because of inefficiencies in the ID or in the case of very hard bremsstrahlung in the first few layers of the ID. For example, 0.8% of 40 GeV electrons have less than 0.5 GeV when entering the TRT. While it is essential to reduce the electron mis-identification, it is important not to lose too much in photon efficiency, since the photons have a significant conversion probability. A photon may be mis-identified as an electron if it converts early in the detector and only one track is seen, or if a fake or unrelated track points by chance to the corresponding EM cluster.

To ensure a high rejection of electrons, an algorithm was developed which used two separate pattern recognition programs in the ID. This enabled the weaknesses of one program to be compensated by the other, and vice versa. The performance of the algorithm was measured on samples of $H \rightarrow \gamma\gamma$ events with and without high luminosity pile-up and a high statistics sample of $Z \rightarrow ee$ events without pile-up. Additional cross-checks were performed on single electrons both with and without pile-up at high luminosity. This study [7-10] was limited to the fiducial region defined in Section 7.6.2 and to the p_T-range of interest: 25 GeV–100 GeV. Photons were required to satisfy the criteria given in Section 7.6.2, but without the track veto.

7.7.1 Calorimeter reconstruction and matching to the ID

The starting point for the analysis was a 3×7 cluster in the EM Calorimeter. Tracks were searched for in a fairly large cone $\Delta\eta = \pm 0.1$, $\Delta\phi = \pm 0.1$ centred on the direction of the cluster, and the direction of each track found was compared with the position of the cluster. The electron direction measured by the cluster was corrected as described in Section 7.2.2.4. A track was considered as pointing to the cluster if $\Delta\eta < 0.01$ and $\Delta\phi < 0.02$ for a PixlRec track. The window used for xKalman was half the size and for both algorithms it was scaled by a factor $40/E_T$ for E_T less than 40 GeV.

7.7.2 Inner Detector reconstruction

Two complementary pattern recognition programs were used for track reconstruction. Bremsstrahlung recovery was performed in the ID using the ID information alone and not the EM cluster position (see Section 7.2.1.1). The first one, xKalman (see Section 3.1.2) is relatively immune to silicon detector inefficiencies since it is based on TRT hits and is extrapolated to the silicon detectors. However, it is sensitive to hard bremsstrahlung since this is treated as a

continuous noise term in the Kalman Filtering formalism and not as a point-like break in the track curvature. Also xKalman cannot reconstruct tracks which do not reach the TRT or do so but have $p_T < 0.5$ GeV. 2.8% of the electrons are not reconstructed satisfactorily by xKalman. xKalman tracks were selected with $p_T > 1$ GeV, less than 50% missing TRT hits, more than seven silicon hits, and impact parameter multiplied by the sign of the curvature (so that the signed parameter is positive if the beam line and helix axis lie on the same side of the track) between -15σ and $+5\sigma$ were selected.

The second pattern recognition program PixlRec (see Section 3.1.2) builds tracks layer by layer, starting from the *B*-layer. Electrons undergoing hard bremsstrahlung can be recovered, provided they reach the penultimate silicon layer. As the ultimate rejection was provided by PixlRec, less severe requirements were set on PixlRec tracks: $p_T > 1$ GeV, at least two pixel hits and at least seven silicon hits were required.

Tracks found in the search cone associated with the EM cluster were accepted only if they did not form a valid conversion using xConver (see Section 7.5.1.1) with any other opposite charge track. Tight quality cuts were applied on conversions to avoid mis-identifying as photons electrons which had undergone hard bremsstrahlung followed by conversion. xKalman conversions were required to have a χ^2 less than 40 and a p_T in excess of 70% of the E_T of the cluster. PixlRec conversion were required to have a χ^2 less than 10, a p_T between 70% and 120% of the E_T of the cluster; no track associated to a *B*-layer hit if the radius of the conversion is more than 6 cm; and no track with more than 90% of the p_T of the conversion.

7.7.3 Results

The flow of electron and photon events after the calorimeter selection is summarised in Figure 7-44. After xKalman, clusters with one associated track inconsistent with a conversion were classified as electron candidates, otherwise they were passed on to PixlRec. If the events which were passed on were subsequently reconstructed with one associated track inconsistent with a conversion, they were also classified as electron candidates - the remainder being photon candidates.

The acceptance of the algorithm for $Z \rightarrow ee$ at low luminosity was $(0.19 \pm 0.02)\%$ for electrons (see Figure 7-45), hence reaching a rejection (reciprocal of efficiency) of 500, while maintaining a $(96.7 \pm 0.2)\%$ photon efficiency. The performance of the algorithm was independent of luminosity for electrons, while the photon efficiency degraded to $(94.4 \pm 0.5)\%$ at high luminosity (Figure 7-46). 0.02% of the electrons were wrongly assigned to a conversion. A further 0.02% were lost because final state radiation in $Z \rightarrow ee$ displaced the EM cluster away from the track. The rest were not reconstructed by either tracking algorithm, having undergone very hard bremsstrahlung. 0.5% of the photons at high luminosity had clusters which had random tracks from pile-up pointing to them. The majority of the photon efficiency loss arose from failures to tag photon conversions, which increase at high luminosity. The photon efficiency of the algorithm with respect to photons passing the track veto described in Section 7.6.2 was 97.4% at low luminosity and 95.4% at high luminosity.

Lowering the silicon layer inefficiency from the nominal 97% to 90% degraded only slightly the performance of the algorithm. Loosening some of the track quality requirements allowed the same electron rejection to be maintained above 500 while losing a further 1% photon efficiency.

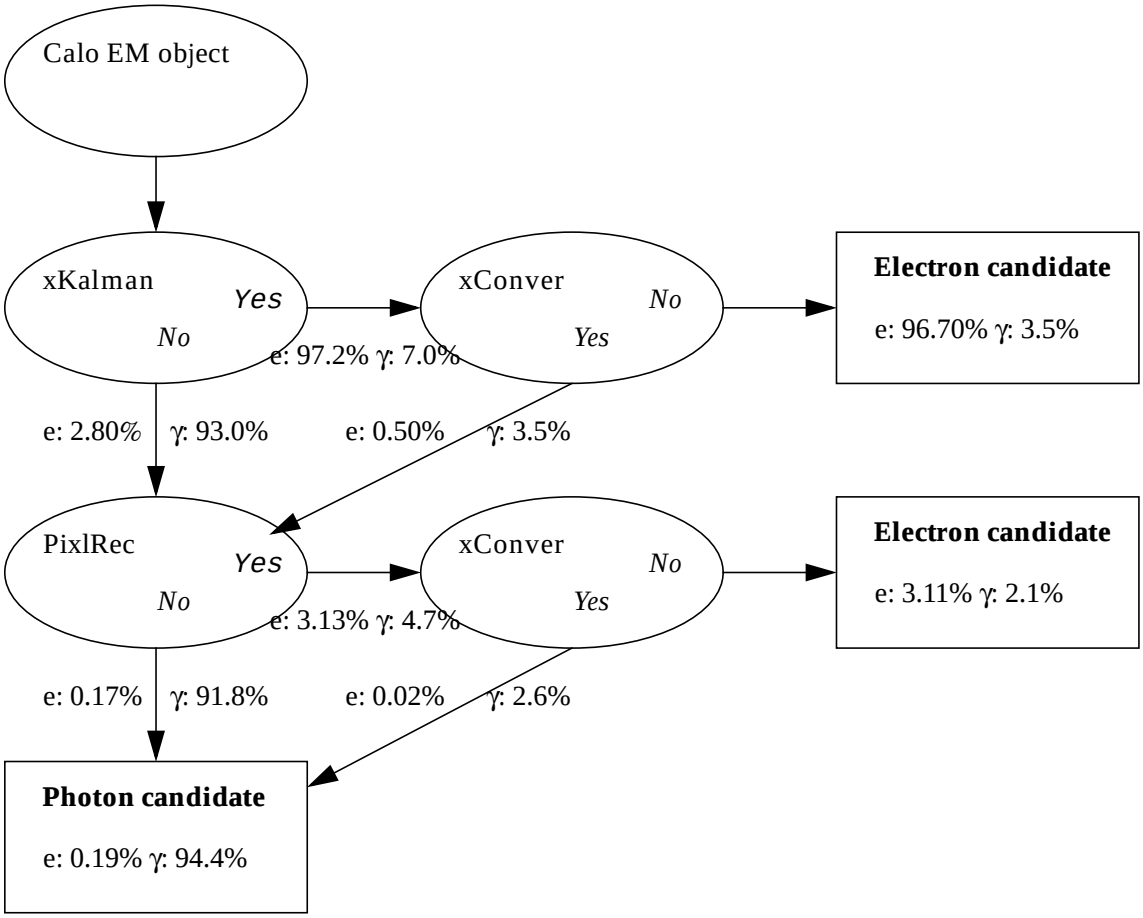

Figure 7-44 Percentages of electrons (e) from $Z \rightarrow ee$ at low luminosity and photons (γ) from $H \rightarrow \gamma\gamma$ at high luminosity which are classified as electron or photon candidates depending on whether tracks have been found ("Yes" or "No") by xKalman and then PixlRec or conversions found ("Yes" or "No") by xConver.

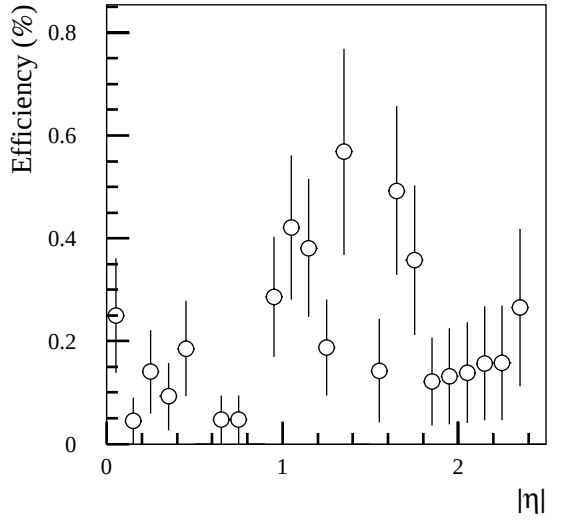

Figure 7-45 Electron efficiency measured on $Z \rightarrow ee$ events. The rejection is the reciprocal of the efficiency.

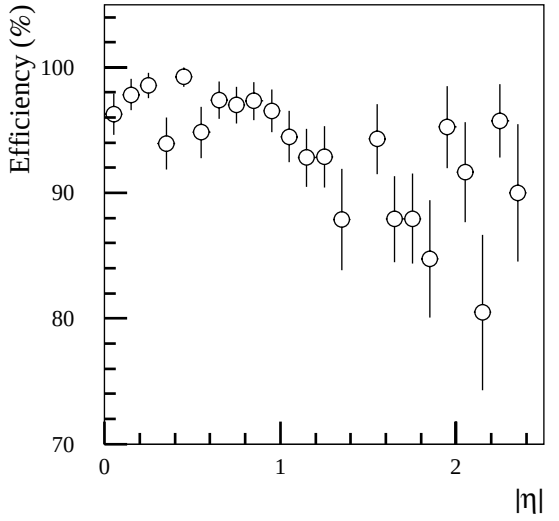

Figure 7-46 Photon efficiency measured on $H \rightarrow \gamma\gamma$ events.

The calorimetric energy of electrons which pass the photon selection is poorly measured since inevitably there is additional energy deposited outside the main EM cluster. The mass resolution of the Z resonance for the mis-identified events is 4.4 GeV (noise and pile-up not included) which is almost four times larger than that of well measured $\gamma\gamma$ pairs. Although $Z \rightarrow ee$ events misidentified as $\gamma\gamma$ pairs will form a peak in the invariant mass distribution, because the cuts described in this section reduce this background to ~10% of the signal and lead to a broader distribution, this background should have little effect on the significance of a possible signal from a low-mass Higgs boson (which lies on top of a much bigger irreducible background) (see Section 19.2.2).

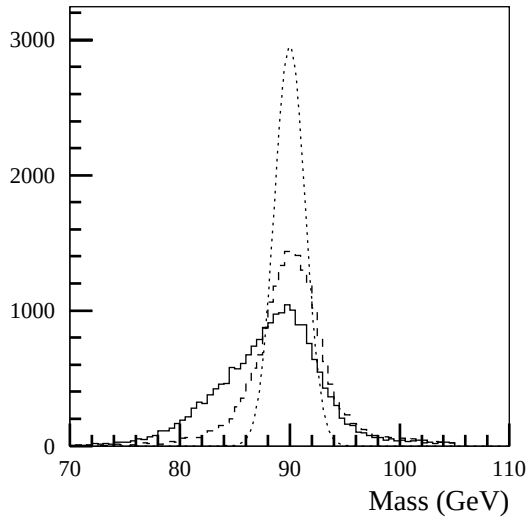

Figure 7-47 $Z \rightarrow ee$ mass resolution for all electrons (dashed), and those electrons mis-identified as photons (solid) compared to the $H \rightarrow \gamma\gamma$ mass resolution (dotted). All histograms are normalised to the same number of events.

7.8 Mass reconstruction

In this section, the mass distributions of important resonances reconstructed through their decays to electrons or photons are presented. The intention is to consider issues associated with the combined reconstruction in the Inner Detector and EM Calorimeter. Of particular concern are the effects of material, noise and their consequences for calibration.

7.8.1 $H \rightarrow \gamma\gamma$

7.8.1.1 Mass resolution

The issues associated with the reconstruction of the $H \rightarrow \gamma\gamma$ channel were discussed in detail in the Calorimeter Performance TDR [7-8]. In this section, an update is given which is based on 10 000 fully simulated $H \rightarrow \gamma\gamma$ events with $m_H = 100$ GeV, and on 10 000 events with $m_H = 130$ GeV.

The event selection required two EM clusters with one having $E_T > 40$ GeV and a second having $E_T > 25$ GeV, both within the pseudorapidity range $|\eta| < 2.4$ (chosen so that the π^0 background could be efficiently reduced). Furthermore, events with one photon pointing to the transition region between the barrel and end-cap EM Calorimeters ($\Delta\eta \sim 0.15$) were rejected. The efficiency of these cuts was 39%. The usual photon identification criteria, corresponding to an overall efficiency of 80% per photon, were then applied as described in Section 7.6.2. This results in an overall acceptance for $H \rightarrow \gamma\gamma$ events of about 25%.

The primary interaction point was reconstructed from the EM Calorimeter alone by a common vertex fit of the two photons, using the constraint provided by the beam-spot: $z = 0$, $\sigma_z = 5.6$ cm. Photon conversions were reconstructed with the xKalman, xHouRec and xConver packages with an efficiency of 80% (see Section 7.5.1.2). Precise vertex position was obtained for 60% of the conversions occurring at a radius less than 45 cm. Figure 7-48 shows the distribution of the reconstructed $\gamma\gamma$ invariant mass. The mass resolution is (1.31 ± 0.05) GeV for $m_H = 100$ GeV. The acceptance in the range of $\pm 1.4\sigma$ around the mass peak is 81% (79%) at low (high) luminosity.

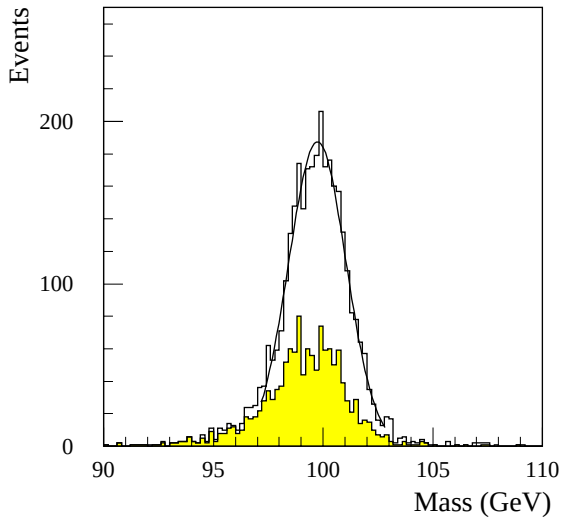

Figure 7-48 Two-photon invariant mass reconstructed in the EM Calorimeter for $H \rightarrow \gamma\gamma$ events with $m_H = 100$ GeV at high luminosity. The open histogram is for all events; the shaded histogram, for events containing at least one converted photon. The fitted curve is a Gaussian with a width of 1.31 GeV.

Table 7-4 shows the various contributions to the Higgs mass resolution, including fully simulated pile-up noise. At low luminosity, digital filtering was applied to reduce the electronic noise. The weights are those computed in the absence of pile-up, and so are independent of the cluster size [7-12]. At high luminosity, the default (hardware) electronic shaping was assumed.

Table 7-4 Breakdown of various contributions to the mass resolution (in GeV) for $H \rightarrow \gamma\gamma$ with $m_H = 100$ and 130 GeV at low and high luminosity.

	$m_H = 100$ GeV		$m_H = 130$ GeV	
	10^{33} cm^{-2}s^{-1}	10^{34} cm^{-2}s^{-1}	10^{33} cm^{-2}s^{-1}	10^{34} cm^{-2}s^{-1}
Sampling term	0.91	0.91	1.07	1.07
Constant term	0.47	0.47	0.65	0.65
Pointing	–	0.47	–	0.57
Pile-up	0.28	0.52	0.23	0.59
Electronic noise	0.19	0.42	0.27	0.42
Total	1.1	1.31	1.3	1.55

At high luminosity, the average pile-up and electronic noise per photon was 930 MeV for $m_H = 100$ GeV. There was a +20% correlation between the two photons which arises from Poisson fluctuations in the number of pile-up events as well as long-range correlations within individual events.

7.8.1.2 Use of the reconstructed primary vertex

To reconstruct the $\gamma\gamma$ mass, it is important to know the position of the primary vertex to obtain the directions of the photons. In principle, greater vertex precision could be achieved by reconstructing the vertex position in the ID when the information is available. The ID information is

fairly unambiguous at low luminosity, but care must be taken not to use the wrong vertex at high luminosity. This possibility was studied by using general assumptions about vertexing. Any vertexing algorithm can be characterised by the efficiency ε_{HV} to find the $H \rightarrow \gamma\gamma$ vertex, and by the average number N_{BV} of additional background vertices arising from the pile-up of minimum bias events. This was studied using a simple Monte Carlo simulation whereby vertices were distributed according to ε_{HV} and N_{BV} along the beam line around $z = 0$. The vertex which was closest to the calorimeter prediction was the one chosen as the candidate for the $H \rightarrow \gamma\gamma$ vertex and used to recompute the photon directions. The calorimeter pointing information reduces the risk of picking a wrong vertex, but cannot eliminate it. Figure 7-49 shows the change in the statistical significance of a Higgs signal, as a function of both ε_{HV} and N_{BV}, as compared to what would be achieved by using the EM Calorimeter alone. Large values of N_{BV} are equivalent to no ID information at all, because under such circumstances there will always be a vertex very close to the calorimeter prediction. The upper left corner of the figure, $\varepsilon_{HV} \sim 1$ and $N_{BV} \sim 0$, corresponds to the low–luminosity running.

An algorithm to find one or more primary vertices can be implemented in many ways. A very simple algorithm which proceeds in three steps was tested. First, tracks were preselected according to the track quality and a fixed cut on p_{T}. Then tracks were clustered to form vertices, according to their z impact parameter, until the vertex spread reached 0.5 mm. Finally vertices with less than four tracks were rejected. Figure 7-49 shows the values of ε_{HV} and N_{BV} achieved in this way, as a function of the p_{T} preselection cut. The results were based on 400 $H \rightarrow \gamma\gamma$ events which were fully reconstructed in the presence of pile–up in the Inner Detector. For comparison, results obtained at particle–level, which assume 100% track reconstruction efficiency over $|\eta| < 2.5$, are also shown.

The conclusion from Figure 7-49 is that the angular resolution of the EM Calorimeter is already very good and it will be difficult to enhance the significance of a possible $H \rightarrow \gamma\gamma$ signal using the reconstructed primary vertex information - even with a vastly better vertex finder. In principle, it would be possible to tag the $H \rightarrow \gamma\gamma$ vertex by using information such as the number of high-p_{T} tracks associated with the vertex [7-7]. However, such methods are very sensitive to possibly large systematics from the modelling of the minimum bias events and of the p_{T} spectrum of the Higgs boson.

7.8.2 $H \rightarrow eeee$

7.8.2.1 Signal generation and reconstruction

Two samples of fully simulated $H \rightarrow eeee$ events with $m_H = 130$ GeV and $m_H = 170$ GeV were studied. The event generation was done using PYTHIA 5.7 and PHOTOS [7-13], in order to take into account the internal bremsstrahlung (also referred to as ‘final state radiation’) contribution. Full simulation included electronic noise, the effect of the constant term and low or high luminosity pile-up.

Electrons were identified above 7 GeV p_{T} from EM clusters reconstructed in 3×7 cells associated to charged tracks with loose E/p matching. The average electron efficiency was 91%. The electron 3-momentum was obtained from a combination of track and reconstructed calorimeter information. Angles were obtained from the track, and a first estimate of the energy was obtained from the cluster, digital filtering being applied at low luminosity [7-12]. To improve the electron energy measurement using tracking information without introducing tails, the following proce-

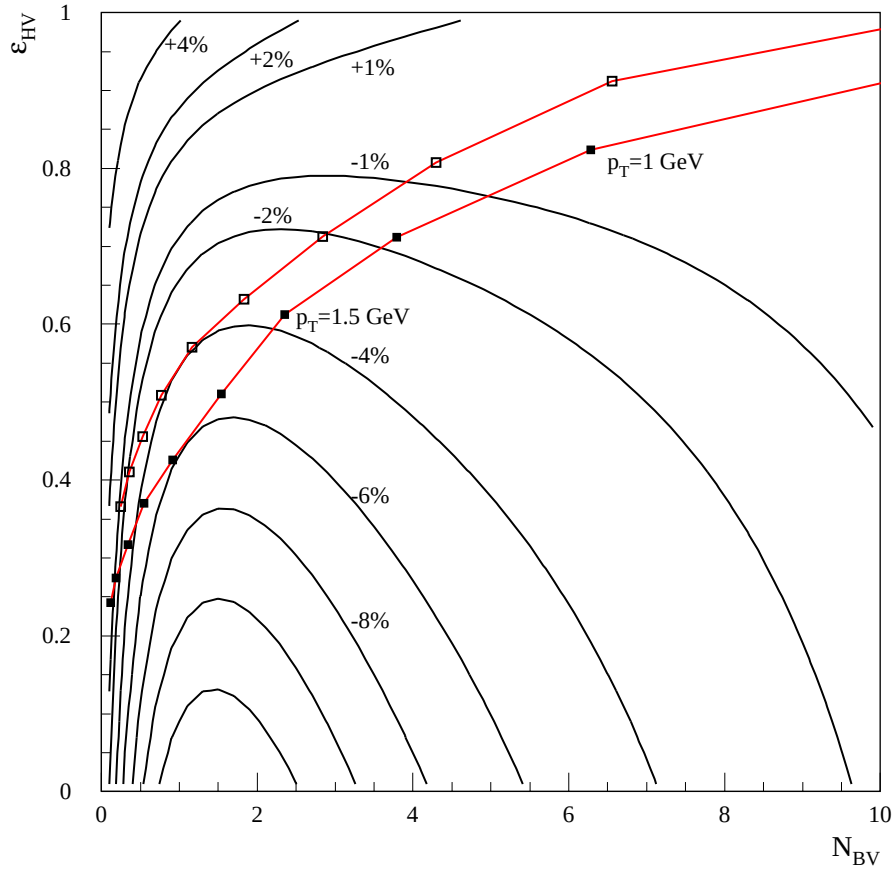

Figure 7-49 Changes in the statistical significance of a possible $H \rightarrow \gamma\gamma$ signal (m_H = 100 GeV) which could be obtained by reconstructing the primary vertex in the ID. The efficiency to reconstruct the Higgs vertex, ε_{HV}, is shown versus the number of reconstructed background vertices, N_{BV}. The contours show the change compared to using the EM Calorimeter information alone. Also shown are the results obtained for one particular vertex finding algorithm in the presence of pile-up at high luminosity, obtained with full simulation and reconstruction (black squares) and at particle-level (open squares), where the squares correspond to different p_T threshold applied in the algorithm.

dure was applied. If the track was consistent with coming from the beam-line within 3σ and had a *B*-layer hit, it was refitted using the vertex and cluster position constraint (bremsstrahlung recovery - see Section 7.2.1). If the refit was successful and the refitted p_T uncertainty less than 6%, the track p_T and its uncertainty were rescaled in such a way as to avoid biases in the estimate. If the track and cluster p_T differed by more than 3σ, the uncertainty on the track p_T was increased so that the discrepancy was exactly 3σ. Finally, a weighted mean of the track and cluster p_T was formed. This procedure enabled the p_T resolution of 60% of the electrons to be improved and was particularly effective at high luminosity.

Kinematical cuts were applied as described in Section 19.2.5, mass cuts being optimised as a function of m_H to maintain good acceptance. A *Z* mass constraint was applied when the mass of an electron pair was within 6 GeV of the *Z* mass. The constraint was imposed by minimising, as a function of the lepton momenta, a χ^2 involving the measured momenta and their uncertainties, as well as the *Z* mass and its natural width. This improved the Higgs mass resolution by 10%.

The mass resolution, obtained from a Gaussian fit in a window [–1.5σ,+2.5σ], was 1.54 GeV (1.97 GeV) at low luminosity (see Figures 7-50 and 7-51) and 1.81 GeV (2.17 GeV) at high luminosity for m_H = 130 GeV (m_H = 170 GeV). The acceptance in the ±2σ mass window was (83.3 ± 0.6)% ((84.7 ± 0.6)%) at low (high) luminosity for m_H = 130 GeV. Similar numbers were obtained for m_H = 170 GeV. Using the momenta measured in the ID improved the mass resolution by 100 MeV at low luminosity and 200 MeV at high luminosity for both Higgs masses.

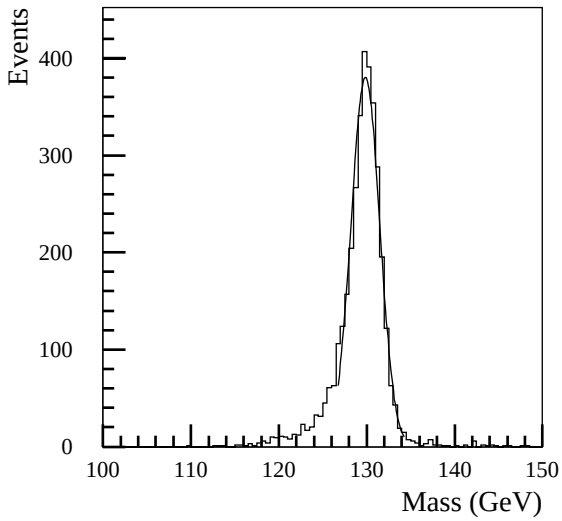

Figure 7-50 Four-electron invariant mass (low luminosity noise and pile-up included) for m_H = 130 GeV.

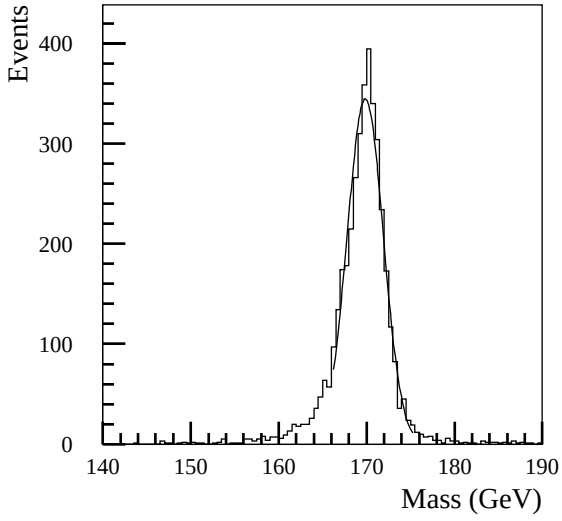

Figure 7-51 Four-electron invariant mass (low luminosity noise and pile-up included) for m_H = 170 GeV.

In contrast to the $H \rightarrow \gamma\gamma$ reconstruction, electrons in the crack region were used. These events had lower identification efficiency and somewhat poorer resolution: in the original ±2σ mass window, the acceptance fell by 7% while the mass resolution for these events was 100 MeV worse (see Figure 7-52). Rejecting these events with one electron in the crack would reduce the final yield in the mass window by 16%.

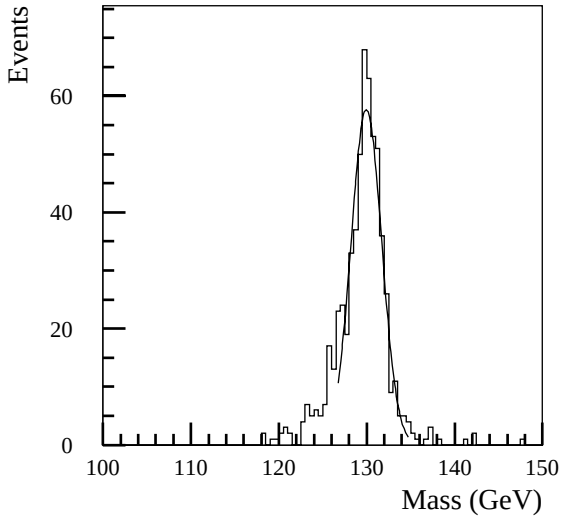

Figure 7-52 Four-electron invariant mass (low luminosity noise and pile-up included) for m_H = 130 GeV, at least one electron being in the crack region.

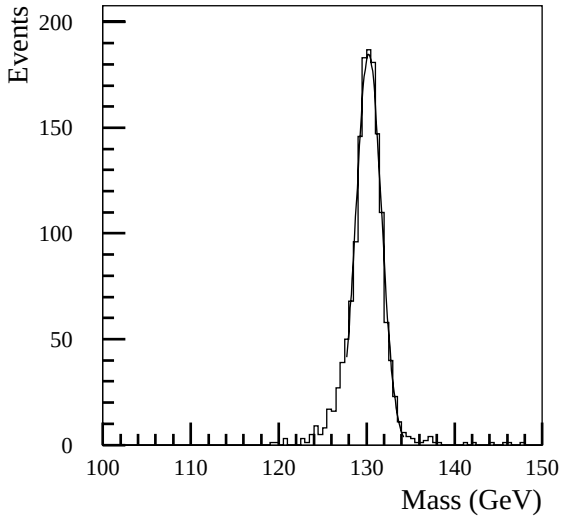

Figure 7-53 Four-electron invariant mass (low luminosity noise and pile-up included) for m_H = 130 GeV, without inner bremsstrahlung.

7.8.2.2 Inner bremsstrahlung contribution

When the inner bremsstrahlung contribution was considered, in most cases the emitted photon lay in the same cluster as the electron and hence the photon was taken into account automatically. For hard photons ($E_T > 5$ GeV) which were not contained in an electron cluster, their energy was added to the closest electron in ΔR [7-14] [7-15]. Inner bremsstrahlung degraded the mass resolution by 100 MeV and decreased the fraction of events in $\pm 2\sigma$ by 3%. Figure 7-53 shows the mass spectrum without inner bremsstrahlung, to be compared to Figure 7-50. In addition, the reconstruction efficiency fell by 9%, giving an overall loss of 12% in acceptance, due to the inner bremsstrahlung contribution.

7.8.2.3 Effect of material in front of the EM Calorimeter

The effect of material in front of the EM Calorimeter can be understood from studies which considered layouts where one Pixel layer or one SCT layer was removed [7-16]. These studies cannot be compared directly with the current ones because of different kinematical cuts. The effect on the acceptance in a $\pm 2\sigma$ mass window is shown in Table 7-5 (the same value of σ was used for all three layouts). While the effects of removing a layer in the ID were not huge, it can be seen that the effect of removing a Pixel layer was much more than that of an SCT layer (they are of comparable thickness), indicating that the material at low radius is the most critical.

Table 7-5 Acceptance for $H \rightarrow eeee$ ($m_H = 130$ GeV) in a $\pm 2\sigma$ mass window for the standard ID layout and reduced layouts.

	Acceptance (%)		
	Standard	**Remove SCT layer**	**Remove Pix layer**
No Inner Brem.	86.2 ± 1.5	88.3 ± 2.0	89.0 ± 1.6
All Events	81.0 ± 1.5	82.6 ± 2.0	85.1 ± 1.5

7.8.2.4 Contributions to the mass resolution

The contributions to the four electron invariant mass resolution are shown in Table 7-6. The contributions to the mass resolution are different from the $H \rightarrow \gamma\gamma$ case because of the different p_T spectra of leptons and photons. For $m_H = 130$ GeV, there is one (two) electron with p_T less than 20 GeV in 95% (46%) of the cases, while the photon p_T spectrum starts at 25 GeV in the $H \rightarrow \gamma\gamma$ decays. The acceptance in the $\pm 2\sigma$ mass window departs from the theoretical 95% because of a number of effects. At low luminosity and for $m_H = 130$ GeV, the 12% additional acceptance loss is made up of: 5% from events for which the reconstructed Z mass is more than 6 GeV from the nominal mass causing the Z mass constraint not to be applied, 3% from events with internal bremsstrahlung, 1% from events with one electron in the crack region and 3% from other effects, mainly bremsstrahlung in the Inner Detector.

7.8.3 $J/\psi \rightarrow ee$

In many collider experiments, the decays of the J/ψ and Υ are valuable for calibrating detectors, and in particular electromagnetic calorimeters (see for example [7-1]). For ATLAS, the most important physics requiring precise electron measurement will be in the tens of GeV range. For this, the copious production of $Z \rightarrow ee$ will be more suitable, as described in Chapter 4. Never-

Table 7-6 Contributions to the four electron invariant mass resolution for $H \rightarrow eeee$ (m_H = 130 GeV). Inner bremsstrahlung, a Z mass constraint and combined Inner Detector track and calorimeter p_T measurements are used.

Term	Contribution (GeV)	
	Low luminosity	High luminosity
Sampling term	1.42 ± 0.05	
Constant term	0.36	
Noise	0.44	0.65
Pile-up	0.10	0.85
Total	1.54 ± 0.06	1.81 ± 0.06

theless, it is important to cross-check the calorimeter calibration and to ensure its linearity. This can be achieved by using the lower energy electrons produced by J/ψ decays. The emphasis of the preliminary study presented in this section is on the calibration; the reconstruction of $J/\psi \rightarrow ee$ decays in the context of B physics is discussed in Section 17.2.2, where it is shown how to obtain the optimal signal using electron reconstruction and vertexing in the Inner Detector.

The $J/\psi \rightarrow ee$ final states originate mainly from $b\bar{b}$ decays, since the semi-muonic decay of the other b-quark, $b \rightarrow \mu X$, is required to fulfil the LVL1 trigger. No such trigger exists for Υ which is produced predominantly by gluon fusion. The cross-section for $pp \rightarrow b\bar{b}$ with a muon of $p_T > 6$ GeV for the LVL1 trigger and $B \rightarrow J/\psi$ with $J/\psi \rightarrow ee$ is estimated to be 2.2×10^{-4} μb [7-11]. This corresponds to a rate of 0.22 Hz at a luminosity of 10^{33} cm^{-2}s^{-1}.

An initial study was made using fully simulated $b\bar{b}$ events at low luminosity in which one B hadron was forced to decay to a muon of $p_T > 6$ GeV and the other B hadron was forced to decay to a J/ψ, which in turn was forced to decay to electrons. The electrons were identified using the method described in Section 7.3. The electron candidates were required to satisfy some basic track quality cuts, have $p_T > 0.5$ GeV and have some minimum value of the discriminating function. The invariant mass of pairs of electrons and positrons was formed using the reconstructed tracks. Candidates were selected in the mass window 2.7 to 3.2 GeV.

In the triggered events, there will be a large combinatorial background from pairs formed from Dalitz decays and conversion electrons as well as misidentified pions. It is not clear what background can be tolerated for calibration purposes. Significant improvements in the rejection will be provided by cuts which are sensitive to the B lifetime in the signal events, as shown in the J/ψ analysis in Section 17.2.2.

The J/ψ mass can be determined from the electron energies and directions. For calibration purposes, the energy will be taken from the EM Calorimeter. The directions could be taken from the more accurate measurements provided by the ID, albeit with a potential problem of biassing the ID track direction by bremsstrahlung. Figure 7-54 shows the reconstructed mass using the ID to provide track directions. The resolution is 450 MeV. Electronic noise has been included in the EM Calorimeter response and degrades the resolution by 110 MeV. Using the EM Calorimeter energy results in a lower reconstructed J/ψ mass due to energy losses, in particular those arising from bremsstrahlung where the radiated photons are not included in the main cluster.

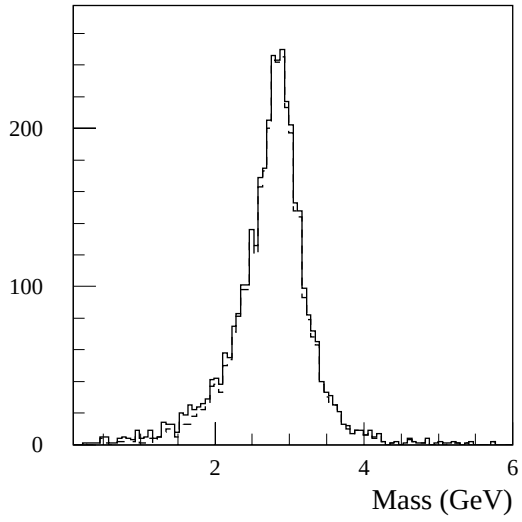

Figure 7-54 Invariant mass of $J/\psi \rightarrow ee$ candidates - the dashed histogram corresponds to real J/ψ decays. To form the mass, the energies of the electrons are taken from the EM Calorimeter and the directions from the ID.

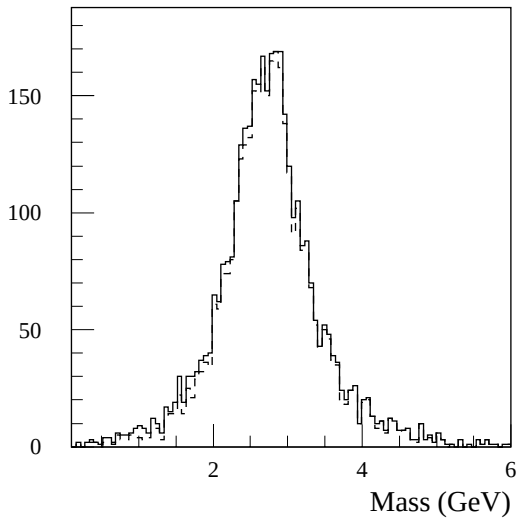

Figure 7-55 Invariant mass $J/\psi \rightarrow ee$ candidates - the dashed histogram corresponds to real J/ψ decays. To form the mass, the energies and directions of the electrons are taken from the EM Calorimeter.

One may want to determine the mass purely from the EM Calorimeter to control systematic uncertainties. Figure 7-55 shows the reconstructed mass using the EM Calorimeter only. The resolution is 600 MeV, the electronic noise contributing with 200 MeV. In one year of low luminosity running (10 fb^{-1}), one can expect 4.4×10^5 reconstructed $J/\psi \rightarrow ee$ decays, assuming a 20% reconstruction efficiency. With a mass resolution of ~20%, this allows a calibration of the ~400 motherboard regions ($\Delta\eta\times\Delta\phi = 0.2\times0.4$) of the EM Calorimeter at low energy to a statistical precision of 0.6%. Future study is needed to obtain a better understanding of the rejection of the background, the $J/\psi \rightarrow ee$ reconstruction efficiency and the consequences of residual combinatorial background.

7.9 Conclusions

The combination of the Inner Detector and the EM Calorimeter provides the potential to identify and measure the energy of electrons and photons in the presence of the known backgrounds. This will enable ATLAS to achieve the physics goals identified in subsequent chapters.

Electrons and photons are significantly affected by the material in front of the EM Calorimeter. Nevertheless, the effects of bremsstrahlung and conversions can be partially compensated for by a number of methods indicated in this chapter. Using E/p from $W \rightarrow e\nu$ events, it should be possible to calibrate the EM Calorimeter in 400 regions ($\Delta\eta\times\Delta\phi = 0.2\times0.4$) to 0.1% after one week of low luminosity running. In the same regions, it should be possible to calibrate at low energy using $J/\psi \rightarrow ee$ to 0.6% after one year, although the background remains to be studied.

Low energy electrons coming from $b \rightarrow eX$ or $J/\psi \rightarrow ee$ can be identified. At higher energies, $E_T > 20$ GeV, an electron efficiency of ~70% can be achieved with a corresponding jet rejection of ~10^5, resulting in an inclusive electron sample of electrons from W/Z decays and heavy flavour. For a photon efficiency of ~80%, a jet rejection of ~1000 (~3000) can be achieved for $E_T \approx 20$ (40) GeV - the remaining jet sample being dominated by isolated EM particles.

The mass resolution for a light Higgs boson ($m_H = 100$ GeV) decaying to two photons is 1.1 (1.3) GeV at low (high) luminosity, while the mass resolution for the four electron decay ($m_H = 130$ GeV) is 1.5 (1.8) GeV. Electrons from Z decays can be sufficiently well identified so as not to constitute a serious background to a possible nearby Higgs boson signal.

7.10 References

7-1 CDF Collaboration, Phys. Rev. **D52** (1995) 4784.

7-2 P. Pralavorio, 'Electron / Jet Separation with the ATLAS Detector', ATLAS Internal Note ATL-COM-PHYS-99-045 (1999).

7-3 A. Dell'Acqua *et al.*, '1997 ATLAS Jet Production', ATLAS Internal Note PHYS-NO-102 (1997).

7-4 M. Wielers, 'Photon Detection with the ATLAS Detector', ATLAS Internal Note ATL-COM-PHYS-99-011 (1999).

7-5 Particle Data Group, The European Physical Journal **C3** (1998) 1.

7-6 ATLAS Collaboration, Inner Detector Technical Design Report Vol. I, CERN / LHCC 97-16 (1997).

7-7 U. Egede, PhD. Thesis, Lund University LUNFD6 / (NFFL-7150) (1997).

7-8 ATLAS Collaboration, Calorimeter Performance Technical Design Report, CERN / LHCC 96-40 (1996).

7-9 E. Richter-Was *et al.*, 'ATLFAST 1.0 A Package for Particle-level Analysis', ATLAS Internal Note PHYS-NO-079 (1996).

7-10 D. Rousseau, 'Electron / Photon Separation', ATLAS Internal Note INDET-NO-198 (1998).

7-11 M. Smizanska *et al.*, 'Overview of Simulations for ATLAS *B* Physics Studies in Period 1996-1999', ATLAS Internal Note ATL-COM-PHYS-99-042.

7-12 S. Simion, 'Pile-up Simulation for ATLAS Calorimeters', ATLAS Internal Note ATL-COM-SOFT-99-001 (1998).

7-13 Z. Was *et al.*, Comput. Phys. Commun. **79** (1994) 291.

7-14 O. Linossier and L. Poggioli, 'Final-state Inner-bremsstrahlung Effects on $H \rightarrow ZZ^* \rightarrow 4l$ with ATLAS', ATLAS Internal Note PHYS-NO-75 (1995).

7-15 O. Linossier and L. Poggioli, '$H \rightarrow ZZ^* \rightarrow 4l$ Channel in ATLAS', ATLAS Internal Note PHYS-NO-101 (1997).

7-16 D. Barberis *et al.*, 'A Comparative Study of Reduced Layouts of the ATLAS Inner Detector', ATLAS Internal Note INDET-NO-188 (1997).